Geochemistry, Geophysics, Geosystems

RESEARCH ARTICLE
10.1029/2020GC009032

This article is a companion to Holt and Royden (2020), https://doi.org/10.1029/2019GC008771.

Key Points:
- This paper presents an analytical method for determining dynamic pressures for simple and complex plate geometries in Cartesian and spherical domains
- Discontinuities in regional dynamic pressure across slabs are directly linked to slab dip via a force balance involving slab buoyancy
- Simple plate/slab geometries and velocities produce readily quantifiable regional velocity and dynamic pressure fields

Supporting Information:
- Supporting Information S1

Correspondence to:
L. H. Royden,
lhroyden@mit.edu

Citation:
Royden, L. H., & Holt, A. F. (2020). Subduction dynamics and mantle pressure: 1. An analytical framework relating subduction geometry, plate motion, and asthenospheric pressure. *Geochemistry, Geophysics, Geosystems*, *21*, e2020GC009032. https://doi.org/10.1029/2020GC009032

Received 17 MAR 2020
Accepted 6 MAY 2020
Accepted article online 16 MAY 2020

Subduction Dynamics and Mantle Pressure: 1. An Analytical Framework Relating Subduction Geometry, Plate Motion, and Asthenospheric Pressure

Leigh H. Royden[1] and Adam F. Holt[1,2]

[1]Department of Earth, Atmospheric, and Planetary Sciences, MIT, Cambridge, MA, USA, [2]Rosenstiel School of Marine and Atmospheric Sciences, University of Miami, Miami, FL, USA

Abstract Recent work suggests that slab dip may be controlled by differences in dynamic pressure above and below the slab at mid-asthenospheric depth, motivating exploration of how plate and slab motion are linked to dynamic pressure in the asthenosphere. This paper, the first of two companion papers, presents an analytical method for determining dynamic pressure and velocity in a thin asthenospheric channel, with linear viscosity, consistent with prescribed plate and slab kinematics. Slabs are explicitly incorporated as vertical barriers to asthenospheric flow. Dynamic pressure is expressed as sums of functions with two functional forms, P_{edge} and P_{wall}; the former generates discontinuities in velocity (but not pressure) at non-slab boundaries, and the latter generates discontinuities in pressure (but not velocity) at boundaries with slabs. Application to simple rectangular plate systems demonstrates that asthenospheric velocities within about one trench length of slabs are insensitive to processes on the opposing side of the slab, that dynamic pressure scales linearly with trench length for a given plate aspect ratio and scales approximately linearly with the shortest plate dimension. Although dynamic pressure is quasisymmetrical across convergent plate boundaries that lack slabs, the presence of slabs creates discontinuity and asymmetry in dynamic pressure across subduction zones. When flux of asthenosphere into the lower mantle occurs adjacent to subducting slabs, dynamic pressure is decreased on the side of the slab where down-flux occurs. This analytical method, applied to systems with multiple arbitrarily shaped plate boundaries, yields excellent results as benchmarked against 3-D numerical solutions.

1. Introduction

The potential energy associated with subducting slabs composed of old oceanic lithosphere is, measured per unit trench length and relative to the surrounding upper mantle, approximately 15 times larger than that associated with buoyancy forces at mid-ocean ridges (e.g., Forsyth & Uyeda, 1975). Stresses transmitted along slabs and into adjacent plates regulate the rate of plate motion, which is in turn coupled to flow in the asthenosphere via shear stresses at the base of the plates. Slabs also form physical barriers in the upper mantle, impeding and organizing lateral flow in the asthenosphere.

A vast body of work has focused on constraining mantle flow by combining numerical models with observational data, but only a small fraction of the work has focused on how subduction observations are related to mantle flow regime (e.g., Alisic et al., 2012; Hager & O'Connell, 1978; Husson, 2012). Early work by Stevenson and Turner (1977) demonstrated that local mantle flow above a descending slab, and the resulting dynamic pressure, provides an upward force on the slab and plays a role in determining slab dip at shallow depth. Subsequent efforts to explain slab dip at deeper, mid-upper mantle depths using regional observations, including slab buoyancy, trench length, plate size, and convergence rate, have been largely unsuccessful (e.g., Cruciani et al., 2005; Jarrard, 1986; Lallemand et al., 2005). This suggests that some of the fundamental processes related to subduction, and its interaction with viscous flow in the asthenosphere, are not yet understood.

Early global flow models by Hager and O'Connell (1978), which imposed observed plate motions as a surface boundary condition, demonstrated mantle flow trajectories that were within about 15° of observed slab dip at the major subduction zones. Their results suggest that there is a link between the dynamic pressure

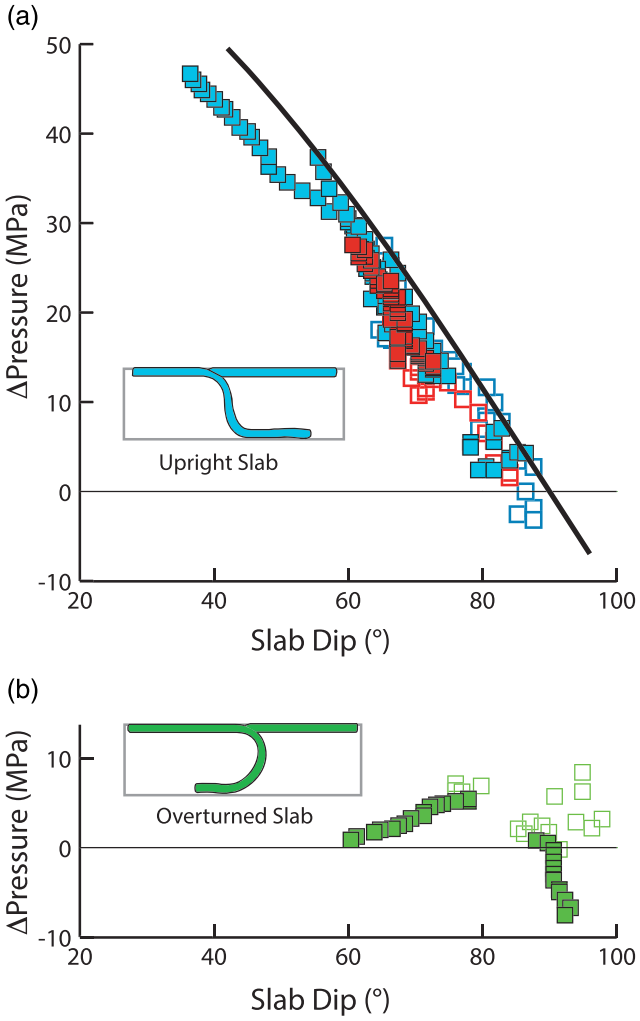

Figure 1. (a) Slab dip versus difference in dynamic pressure above and below the slab at mid-upper mantle depth, from numerical models of single (red) and double (blue) subduction systems (Holt et al., 2017). Black line shows theoretical relationship if slab-normal component of buoyancy supported the dynamic pressure difference. (b) Same but for slabs overturned onto the base of the upper mantle. (Solid squares represent dips for near-steady state subduction geometry, open squares represent early subduction stages with rapidly evolving slab geometries.)

associated with mantle flow and slab dip, but did not contain slabs. Subsequent analog and numerical modeling studies of subduction-induced mantle flow on a regional scale have shown that horizontal motion of a subducting slab promotes toroidal flow around the slab edges, from regions of high pressure to regions of low pressure (e.g., Buttles & Olson, 1998; Funiciello et al., 2004; Kincaid & Griffiths 2003; Schellart 2004; Stegman et al., 2006).

Recently, Holt et al. (2017) used 3-D, time-evolving numerical models of single and double subduction systems to demonstrate that the difference in dynamic pressure across a slab at mid-asthenospheric depth is approximately equal to what is needed to support the slab-normal component of the slab buoyancy force (Figure 1, with additional points for wider, 4,000 km, trench added using identical computational method). This offers the possibility that slab dip can be used as a measure of dynamic pressure within the asthenosphere and motivates exploration of how plate and slab motion are linked to dynamic pressure.

This paper is the first of two companion papers that explore the relationship among asthenospheric pressure, plate-slab geometry and velocity, and ultimately, Earth's global pattern of slab dips. Here, we develop an analytical approach for quantifying the relationship between plate-slab motions and dynamic pressure in the asthenosphere. The goal is to develop intuition about how plate and slab motions are related to dynamic pressure in the asthenosphere and to build a tool that can be used with any plate and slab geometry. The companion paper (Holt & Royden, 2020) explores the connection between the globally observed plate and trench geometry and velocities, and slab dip. We begin with the development of our analytical method (sections 2 and 3) and then apply it to simple plate and slab configurations to develop basic intuition about how various processes affect the pressure and velocity fields (section 4). We then adapt the method for use in systems with arbitrarily configured plate and slab geometries and compare our results to 3-D numerical solutions (section 6).

2. Analytical Approach to Flow in the Upper Mantle

Analytical approaches provide a useful complement to numerical methods through equations that describe, or approximate, the behavior of a system at large scale, offering useful insights into system-wide behaviors. Because nearly all modeling of regional and global mantle flow is numerical, there is need for analytical approaches to complement the numerical results. Compared to numerical methods, analytical solutions are generally very fast to implement computationally, allowing for exploration on scales that may not yet be amenable to numerical methods, or allowing for multiple analyses to be performed in short periods of time. Here, we develop a mathematical method, based on concepts presented in Royden and Husson (2006), to determine asthenospheric pressure and velocity from known plate and slab geometries and velocities.

We follow Royden and Husson (2006) in dividing the full 3-D problem of asthenospheric flow into two coupled components: (1) a regional flow solution that describes upper mantle flow except within a few hundred kilometers of the subducting slabs and (2) a local flow solution near the slab region that adds an additional component of dynamic pressure, but with significant effect on dynamic pressure only in a narrow portion of the asthenospheric wedge above the slab (Figure 2). Here, we focus on the first component, computing the asthenospheric velocities and upper mantle pressures that are consistent with a priori specified trench and plate geometries and velocities. (In the companion paper, the regional flow component of flow is scaled up to include the entire Earth, and those solutions are referred to as

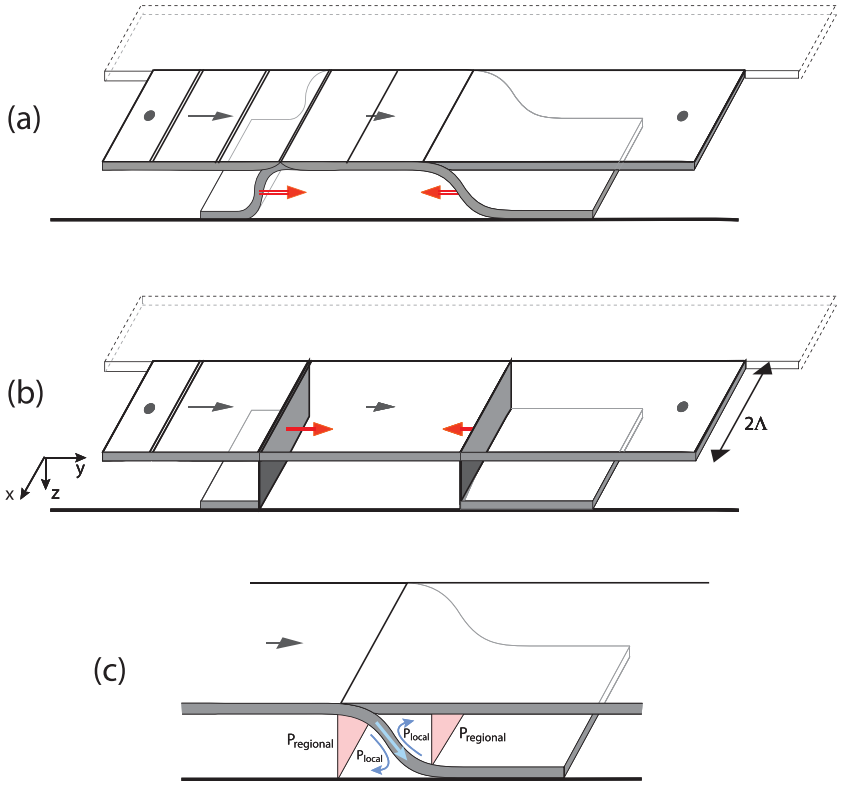

Figure 2. Sketch showing how the geometry of subduction systems (a) is simplified in our analytical models (b) and how the pressure solution is separated into regional and local components (c). In the idealized regional subduction framework, slabs are treated as rigid vertical walls. Plate systems have stationary side plates, with one side plate shown in panels (a) and (b).

"global" solutions. In this paper, we use the term regional to include all the plates and slabs within the model domain.)

To avoid cumbersome terminology, we will refer to the upper mantle, excluding plates and slabs, as "asthenosphere." "Pressure" will be used to mean dynamic pressure. We determine dynamic pressure from total pressure by subtracting from it the pressure at an equivalent depth in a hydrostatic column of asthenosphere beneath a mid-ocean ridge.

3. Hele-Shaw Approximation for Pressure and Velocity

We use a Hele-Shaw-type approximation for flow in a thin planar channel containing a linear viscous material. Hele-Shaw flow is characterized by irrotational (or pressure-driven) flow on horizontal (x-y) planes (i.e., the curl of the stream function is zero) and dynamic pressure that is uniform with depth (Batchelor, 2000). The main shortcoming of Hele-Shaw approximations, and all forms of irrotational flow, is that only the boundary-normal component of velocity can be constrained at lateral boundaries like slabs; the boundary-parallel component of velocity is unconstrained at all boundaries. However, Hele-Shaw flow provides a good approximation for flow at length scales comparable to and greater than about half the channel depth (see analysis in section 5).

Within our analytical framework, slabs are introduced as barriers to asthenospheric flow and treated as rigid vertical walls at the location where each slab passes through the mid-depth of the channel (i.e., 330 km, Figure 2b). Each slab wall moves horizontally at the velocity of the corresponding slab profile (which is equal to the trench velocity if slab dip is constant through time). We require the (vertically averaged) velocity of the asthenosphere adjacent to each slab wall to move at the same slab-normal velocity as the slab wall. The slab-parallel component of asthenospheric velocity cannot be constrained.

Table 1
Definition of Variables Used in the Text

Variable[a]	Definition	Comments
$\boldsymbol{v}_{\boldsymbol{p}}(x,y)$	Plate velocity	
a	Asthenosphere thickness	
P	Dynamic pressure	
μ	Viscosity	
τ_{xy}	Shear stress on x-y planes	
x,y	Horizontal coordinates (planar) planes	$x' = x/\Lambda$; $y' = y/\Lambda$
z	Depth	
$\boldsymbol{v}_{\boldsymbol{a}}(x,y,z)$	Asthenosphere velocity	
$\boldsymbol{c}$	Constant of integration	
$f_1 f_2$	Functions of viscosity	Equations (4)–(6)
$\boldsymbol{v}_{\boldsymbol{b}}(x,y)$	Basal (or slab tail) velocity	
C	Viscosity coefficient	Equations (6) and (8)
β	Coupling coefficient	Equations (7) and (8); value is 0 to 1
ℓ	Plate thickness	
ℓ'	Slab tail thickness	
$\overline{\boldsymbol{v}}_{\boldsymbol{a}}(x,y)$	Vertically averaged asthenosphere velocity	
$\overline{\boldsymbol{v}}_{\mathbf{total}}(x,y)$	Vertically averaged upper mantle velocity	
h	Upper mantle thickness	
Λ	Segment half length	See section 3.2
$P_{\text{edge}}(x,y)$	Pressure function (edge boundaries)	Defined in Equation (11)
A	Coefficient modifying P_{edge}	Equation (11)
$\overline{\boldsymbol{v}}_{\mathbf{edge}}(x,y)$	Velocity resulting from P_{edge}	Defined in Equation (12)
$P_{\text{wall}}(x,y)$	Pressure function (wall boundaries)	Defined in Equation (13); see also section SA
B	Coefficient modifying P_{wall}	Equation (13)
$\overline{\boldsymbol{v}}_{\mathbf{wall}}(x,y)$	Velocity resulting from P_{wall}	Equations (14) and (15)
d	Plate length	See Figures 6 and 8; $d' = d/\Lambda$
s	Slab tail length	See Figures 9 and 10; $s' = s/\Lambda$
$\boldsymbol{v}_{\boldsymbol{w}}$	Velocity of slab profile	See Equations (22) and (23) and Figure 7
c	Half separation width between slabs	See Figure 10; $c' = c/\Lambda$
F_{DG}	Asthenosphere flux into the lower mantle	Downgoing plate side of slab, Equations (33) and (34)
F_{OR}	Asthenosphere flux into the lower mantle	Overriding plate side of lab, Equations (33) and (34)

Note. Definition of variables used in the text, excluding variables used only in the supporting information.
[a]Variables in boldface indicate vector quantities.

3.1. General Equations for Pressure and Velocity

We consider a channel of thickness a with upper surface overlain by rigid plates with velocity field $\boldsymbol{v}_{\boldsymbol{p}}(x,y)$, where x-y planes parallel the upper surface of the channel and z is depth (see Figure 2 for coordinate system). (Boldface symbols indicate vector quantities. See Table 1 for summary of variables.) The base of the channel is constrained either to have a specified velocity $\boldsymbol{v}_{\boldsymbol{b}}(x,y)$ ("fixed velocity base") or to have no shear stress ("stress-free base"). Plates are not allowed to deform internally, so that the divergence of $\boldsymbol{v}_{\boldsymbol{p}}$ is zero except across plate boundaries with relative displacements. Within the channel, dynamic pressure is related to shear stress on horizontal planes, $\boldsymbol{\tau}_{\boldsymbol{xy}}$, by

$$\frac{\partial \tau_{xy}}{\partial z} = \nabla P\,(x,\,y). \tag{1}$$

Integrating over z gives the derivative of the horizontal component of (asthenospheric) velocity as a function of depth, $\boldsymbol{v}_{\boldsymbol{a}}$:

$$\mu(z)\frac{\partial \boldsymbol{v}_{\boldsymbol{a}}}{\partial z} = z\,\nabla P + \boldsymbol{c}, \tag{2}$$

where the left-hand side is shear stress expressed in terms of velocity, $\mu(z)$ is viscosity, and $\boldsymbol{c}$ is a constant of integration.

Dividing by μ, integrating again, and setting the velocity at $z = 0$ equal to $\boldsymbol{v}_{\boldsymbol{p}}$ yield

$$\boldsymbol{v}_{\boldsymbol{a}}(x,\,y,\,z) = \nabla P \int_0^z \frac{z\,dz}{\mu(z)} + \boldsymbol{c}\int_0^z \frac{dz}{\mu(z)} + \boldsymbol{v}_{\boldsymbol{p}}. \tag{3}$$

The constant $\boldsymbol{c}$ can be determined for any vertical viscosity structure and basal boundary condition by the following procedure. For a fixed velocity base, let

$$f_1 = \left(\int_0^a \frac{dz}{\mu(z)}\right)^{-1} \qquad f_2 = f_1 \int_0^a \frac{z dz}{\mu(z)}, \tag{4}$$

where a is the thickness of the asthenospheric channel. For a stress-free base, let $f_1 = 0$, $f_2 = a$. Then:

$$\boldsymbol{v}_{\boldsymbol{a}}(x,\,y,\,z) = \nabla P\left(\int_0^z \frac{z\,dz}{\mu(z)} - f_2\int_0^z \frac{dz}{\mu(z)}\right) + \left[f_1(\boldsymbol{v}_{\boldsymbol{b}} - \boldsymbol{v}_{\boldsymbol{p}})\int_0^z \frac{dz}{\mu(z)} + \boldsymbol{v}_{\boldsymbol{p}}\right], \tag{5}$$

where $\boldsymbol{v}_{\boldsymbol{b}}$ is the velocity at the base of the channel. If we define two scalar parameters as functions of the viscosity structure:

$$\frac{1}{C} = \frac{f_2}{a}\int_0^a\int_0^z \frac{dz dz'}{\mu(z')} - \frac{1}{a}\int_0^a\int_0^z \frac{z\,dz dz'}{\mu(z')}, \tag{6}$$

$$\beta = 1 - \frac{f_1}{a}\int_0^a\int_0^z \frac{dz dz'}{\mu(z')}. \tag{7}$$

Then, integrating Equation (5) over z and dividing by a yield the vertically averaged velocity in the asthenosphere, $\overline{\boldsymbol{v}}_{\boldsymbol{a}}$:

$$\bar{\boldsymbol{v}}_{\boldsymbol{a}}(x, y) = -\frac{\nabla P}{C} + \left[\beta\, \boldsymbol{v}_{\boldsymbol{p}} + (1-\beta)\boldsymbol{v}_{\boldsymbol{b}}\right], \tag{8}$$

where C is a "viscosity coefficient" that describes how the average asthenospheric velocity is related to the lateral pressure gradient via Equation (6).

β is a "coupling coefficient" that describes how the vertically averaged asthenosphere velocity is coupled to the upper and lower boundary conditions. β is 1 for a stress-free lower boundary and 0 for a stress-free upper boundary, independent of the viscosity structure in the asthenosphere. Otherwise, β is between 0 and 1 when the upper and lower boundaries of the channel have imposed velocity conditions, and its value depends on the viscosity structure of the asthenosphere via Equations (4) and (7). It is equal to 0.5 for a uniform viscosity asthenosphere with top and bottom velocity boundary conditions.

The expressions for velocity and vertically averaged velocity in Equations (5)–(8) are readily separated into two components. The "pressure-driven" component of flow is linearly proportional to ∇P; it has zero velocity at the top of the channel and either zero velocity (for fixed velocity base) or zero shear stress (for stress-free base) at the base of the channel. The "plate-driven" component of flow (terms in square brackets in Equations 5 and 8) is linearly proportional to a weighted average of the local $\boldsymbol{v}_{\boldsymbol{p}}$ and $\boldsymbol{v}_{\boldsymbol{b}}$.

We add to our formulation terms for a plate with finite thickness, ℓ. Also, some slabs may display a "slab tail," defined as the part of the slab, with thickness ℓ^*, that lies horizontally along the base of the upper mantle, as most clearly observed in tomographic images of the Pacific slab beneath Japan (e.g., Li et al., 2008). (Note that if the velocity of the slab tail is imposed as a boundary condition on the base of the material in the asthenospheric channel, this is done by setting $\boldsymbol{v}_{\boldsymbol{b}}$ to the slab tail velocity).

The vertically averaged velocity through the entire upper mantle is then

$$\bar{\boldsymbol{v}}_{\mathbf{total}}(x, y) = -\frac{\nabla P\, a}{C\, h} + \left[\beta\, \boldsymbol{v}_{\boldsymbol{p}} + (1-\beta)\boldsymbol{v}_{\boldsymbol{b}}\right]\frac{a}{h} + \left(\frac{\ell}{h}\boldsymbol{v}_{\boldsymbol{p}} + \frac{\ell^*}{h}\boldsymbol{v}_{\boldsymbol{b}}\right), \tag{9}$$

where h is the thickness of the upper mantle ($h = \ell + a + \ell'$). Equations (8) and (9) encapsulate the response of the asthenosphere and upper mantle to imposed plate and slab velocities, with any vertical viscosity structure incorporated into only two scalar constants.

Taking the divergence of Equation (9) and requiring that the divergence of $\bar{\boldsymbol{v}}_{\mathbf{total}}$ be zero gives

$$\nabla\cdot\left(\frac{a}{hC}\nabla P\right) = \nabla\cdot\left[\frac{a\beta}{h}\boldsymbol{v}_{\boldsymbol{p}} + \frac{a(1-\beta)}{h}\boldsymbol{v}_{\boldsymbol{b}}\right] + \nabla\cdot\left(\frac{\ell}{h}\boldsymbol{v}_{\boldsymbol{p}} + \frac{\ell^*}{h}\boldsymbol{v}_{\boldsymbol{b}}\right). \tag{10}$$

If we define a "domain" to be a region where C, β, ℓ, ℓ^*, and a are uniform and $\nabla\cdot\boldsymbol{v}_{\boldsymbol{p}}$ and $\nabla\cdot\boldsymbol{v}_{\boldsymbol{b}}$ are zero, then within any single domain, $\nabla^2 P = 0$. Therefore, within any domain, we can describe the pressure distribution within the asthenosphere, and the pressure-driven component of velocity, with a pressure function whose Laplacian (∇^2) is zero. At the boundary between domains, conservation of mass requires the boundary-normal component of $\bar{\boldsymbol{v}}_{\mathbf{total}}$ be continuous (unless there is flux in or out of the lower mantle, see section 4.4). And at slab walls, which form barriers to flow, the boundary-normal component of $\bar{\boldsymbol{v}}_{\boldsymbol{a}}$ must be equal to the boundary-normal vertically averaged velocity imposed on both sides of the slab wall.

3.2. Useful Mathematical Solutions for Asthenospheric Pressure and Flow

Two functional forms are useful for describing asthenospheric pressure and velocity. These have a Laplacian of zero everywhere except beneath a linear boundary segment of length 2Λ. "Edge" functions, P_{edge}, describe the asthenospheric pressure resulting from divergent or convergent plate motion at the plate boundary (Figure 3a). "Wall" functions, P_{wall}, describe the effect of the slab walls that form barriers to the flow (Figure 3b). In the following sections, we define all convergent and divergent boundaries as having a total length 2Λ. (For convenience in the remainder of the paper, we nondimensionalize all position variables by dividing by the half-segment length, so that $x' = x/\Lambda$, $y' = y/\Lambda$, etc.)

3.2.1. Edge Solutions

For any plate boundary segment extending from $x' = 1$ to $x' = -1$ (i.e., a segment with endpoints at $x = \pm\Lambda$; with coordinate system and orientation as shown in Figure 2b), we define the function P_{edge} as

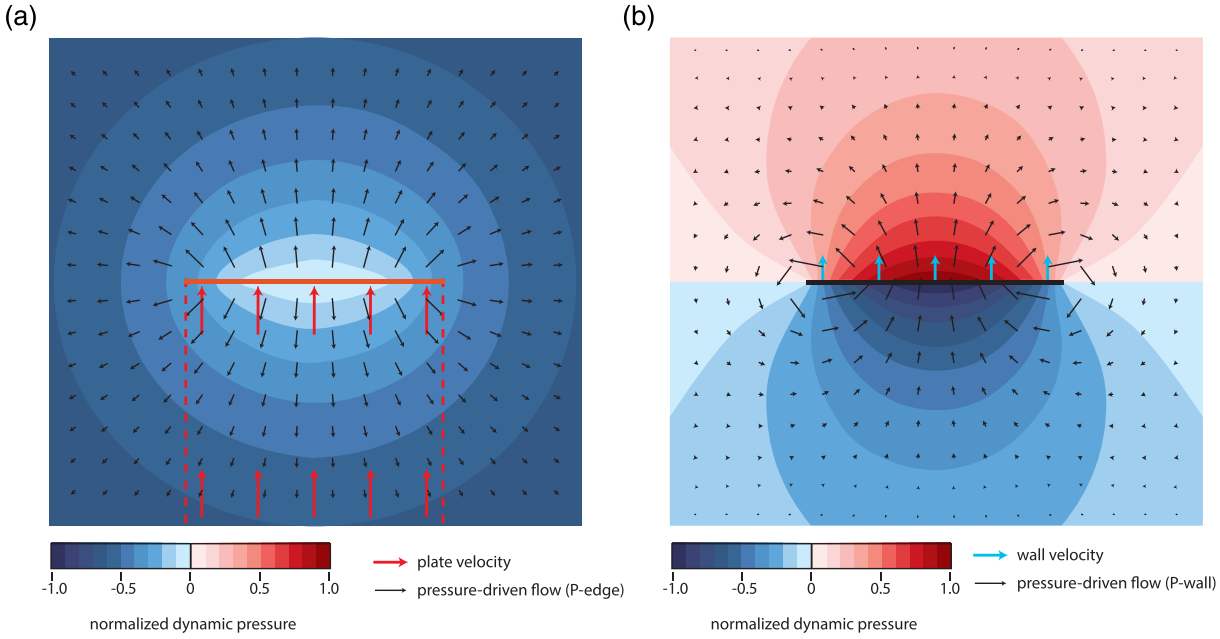

Figure 3. (a) Map view of normalized dynamic pressure (color shading) and vertically averaged channel velocity (black arrows) for P_{edge}, equivalent to convergent boundary without slab (solid red line) bordering a semi-infinite rectangular plate (dashed red outline). (b) Map view of normalized dynamic and vertically averaged channel velocity for P_{wall}, equivalent to a rigid vertical wall (black line) moving as shown by blue arrows, with no plate motion.

$$P_{\text{edge}}(x',y') = A\,\Lambda\,C\left\{\left(\frac{y'}{\pi}\right)\left[\tan^{-1}\left(\frac{x'-1}{y'}\right)-\tan^{-1}\left(\frac{x'+1}{y'}\right)\right] - \left(\frac{1+x'}{2\pi}\right)\ln\left[(x'+1)^2+y'^2\right]+\left(\frac{x'-1}{2\pi}\right)\ln\left[(x'-1)^2+y'^2\right]\right\}, \tag{11}$$

where A is an arbitrary constant with units of velocity. (A is set by the velocity constraints at the associated plate boundary, as described in section 4.)

Later, we will have a need to define P_{edge} functions for multiple plate boundary segments, of arbitrary length and orientation (section 6). If we have n segments, we calculate $P_{\text{edge},n}$ for the nth segment, with segment length $2\Lambda_n$, by defining a temporary coordinate system with origin located at the center of the nth segment and oriented such that the endpoints of the segment are located at $x_n = \pm\Lambda_n; y_n = 0$. $P_{\text{edge},n}$ is calculated in this new coordinate system, and the resulting function translated and rotated back into the original coordinate system. We will refer the resulting pressure distribution as the $P_{\text{edge},n}$ solution that is "centered" around the nth segment boundary.

The vertically averaged velocity in the asthenosphere that results from this pressure field is ∇P_{edge} multiplied by $(-1/C)$:

$$\bar{\boldsymbol{v}}_{\text{edge}}(x',y') = \frac{A}{2\pi}\ln\left[\frac{(x'+1)^2+y'^2}{(x'-1)^2+y'^2}\right]\hat{\boldsymbol{x}} + \frac{A}{\pi}\left[\tan^{-1}\left(\frac{x'+1}{y'}\right)-\tan^{-1}\left(\frac{x'-1}{y'}\right)\right]\hat{\boldsymbol{y}}. \tag{12}$$

Edge functions yield a velocity whose boundary-normal component is uniform along the segment boundary but has opposite sign on either side of the segment (such that positive A corresponds to flow away from the boundary). P_{edge} is continuous across the segment boundary, although its gradient (and associated asthenospheric velocity) is not (Figure 3a).

3.2.2. Wall Solutions

For a plate boundary segment extending from $x' = 1$ to $x' = -1$, we define the function P_{wall} "centered" around this boundary segment as

$$P_{\text{wall}}(x',y') = B\Lambda C\left\{\frac{1}{\sqrt{2}}\frac{|y'|}{y'}\sqrt{\left(y'^2 - x'^2 + 1\right) + \sqrt{\left(y'^2 + x'^2 + 1\right)^2 - 4x'^2}} - y'\right\}, \tag{13}$$

where B is an arbitrary constant with units of velocity. (B is set by the velocity constraints at the associated slab boundary, as described in section 4.) Evaluated along the x and y axes only, the vertically averaged asthenospheric velocities resulting from this pressure field are ∇P_{wall} multiplied by $(-1/C)$:

$$\bar{\boldsymbol{v}}_{\mathbf{wall}}(0, y') = B\left(1 - \sqrt{\frac{y'^2}{1+y'^2}}\right)\hat{\boldsymbol{y}}, \tag{14}$$

$$\bar{\boldsymbol{v}}_{\mathbf{wall}}(x', 0) = B\left[\frac{x'\mathrm{H}\left(1-x'^2\right)}{\sqrt{1-x'^2}}\right]\hat{\boldsymbol{x}} + B\left[1 - \frac{\mathrm{H}(x'^2-1)}{\sqrt{2}}\sqrt{1+\frac{x'^2+1}{\left(x'^2-1\right)^2}}\right]\hat{\boldsymbol{y}}, \tag{15}$$

where H is the Heaviside function.

P_{wall} is discontinuous across the segment boundary and can only be used at boundaries with a slab wall (Figure 3b). P_{wall} produces a uniform velocity B along the segment boundary, with velocity having the same sign on either both sides of the boundary. Thus, P_{wall} shifts the velocities on both sides of the slab wall by a uniform velocity B. In addition, P_{wall} solutions produce a pressure discontinuity at a segment boundary containing a slab wall, $\Delta P = 2B/\Lambda C$. If we have multiple plate boundary segments with slab walls, we create a P_{wall} function for each segment using the same procedure as described for P_{edge} in section 3.2.1. Similarly, we will refer to the $P_{\text{wall},n}$ function, which is derived for the nth segment boundary, as the solution that is "centered" around that nth segment.

(As an aside, expressions related to the P_{wall} function, such as the general velocity expression, are cumbersome in Cartesian coordinates, and functions related to P_{wall} are more easily expressed and manipulated in elliptical coordinates. For the interested reader, an overview of elliptical coordinates and expressions for P_{wall} in elliptical coordinates are given in supporting information section SA.)

4. Pressure Solutions for Simple Plate Boundary Geometries

We apply the solutions P_{edge} and P_{wall} to relatively simple plate configurations in order to build intuition about the interactions among plate/slab geometry, plate velocity, and asthenospheric pressure. To simplify the presentation without compromising fundamental concepts, we set the plate and slab tail thickness, ℓ and ℓ^*, to zero, so that $h = a$ and $\bar{\boldsymbol{v}}_{\boldsymbol{a}} = \bar{\boldsymbol{v}}_{\mathbf{total}}$.

For conceptual purposes, it is helpful to think of the velocity-depth profiles generated by a uniform viscosity fluid with either a fixed velocity or stress-free base. However, the results presented in this section for pressure and vertically averaged velocity are applicable to any vertical viscosity structure, modified for differing values of C and β. For uniform viscosity with a fixed velocity base, C and β can be derived by evaluation of the integrals in Equations (4)–(7): for uniform μ.

$$\boldsymbol{v}_{\boldsymbol{a}} = \frac{\nabla P}{\mu}\left(\frac{z^2 - az}{2}\right) + (\boldsymbol{v}_{\boldsymbol{b}} - \boldsymbol{v}_{\boldsymbol{p}})\frac{z}{a} + \boldsymbol{v}_{\boldsymbol{p}} \qquad C = \frac{12\mu}{a^2} \qquad \beta = \frac{1}{2}. \tag{16}$$

For uniform viscosity with a stress-free base:

$$\boldsymbol{v}_{\boldsymbol{a}} = \frac{\nabla P}{\mu}\left(\frac{z^2 - 2az}{2}\right) + \boldsymbol{v}_{\boldsymbol{p}} \qquad C = \frac{3\mu}{a^2} \qquad \beta = 1. \tag{17}$$

4.1. Plate Boundaries Without Slabs

4.1.1. Single Plate Boundary Without a Slab

We begin with an asthenosphere overlain by a two-plate system, with both plates having zero thickness. One plate covers the domain $|x'| < 1, y' < 0$ with velocity $v_p\hat{\boldsymbol{y}}$ (i.e., moving to the right in Figures 4 and 5). The

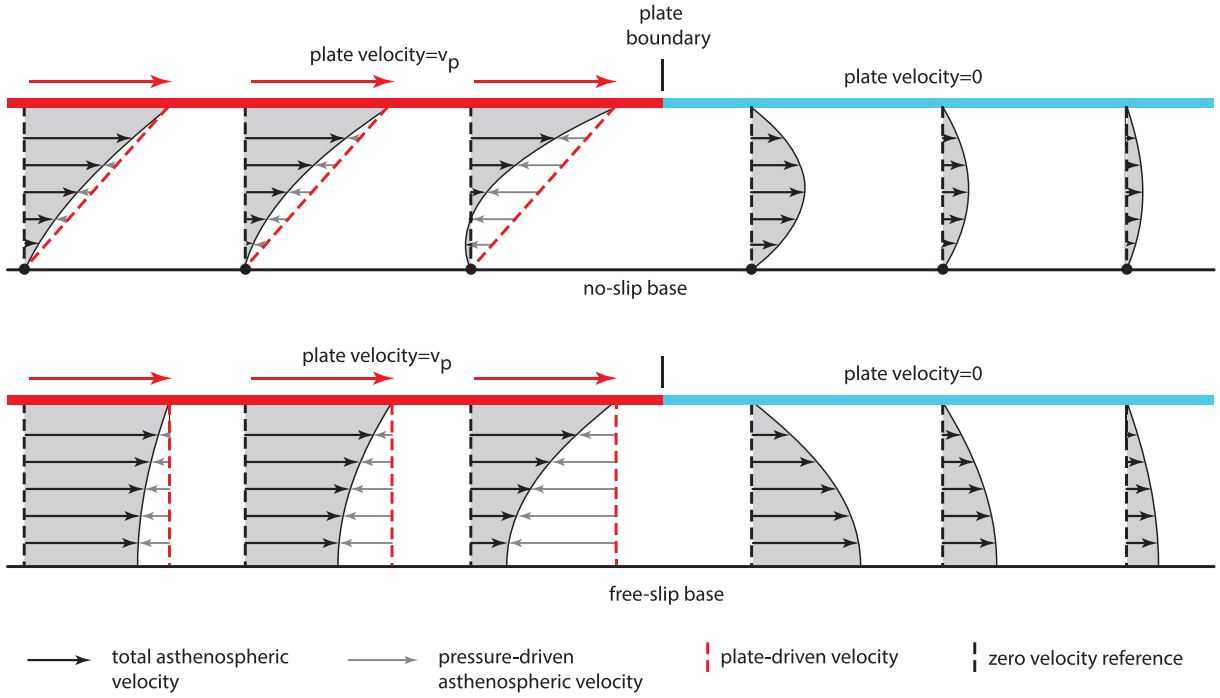

Figure 4. Cross-sectional view of total velocity (black arrows with gray shading), plate-driven flow (dashed red line), and pressure-driven flow (gray arrows) across a convergent boundary without a slab. The left side (red plate) has plate velocity v_p, and the right side has plate velocity of zero, for uniform viscosity with fixed velocity basal boundary condition (top panel) and stress-free basal boundary condition (lower panel).

other plate has velocity $v_o\hat{\boldsymbol{y}}$, with $v_o < v_p$, and occupies the rest of the x-y plane. This yields a convergent boundary at $|x'| < 1, y = 0$.

Because there is no slab wall, we use a solution of form P_{edge} centered on the convergent plate boundary (Equations 11 and 12). (Note that the pressure-driven component of flow is not affected by pure transform

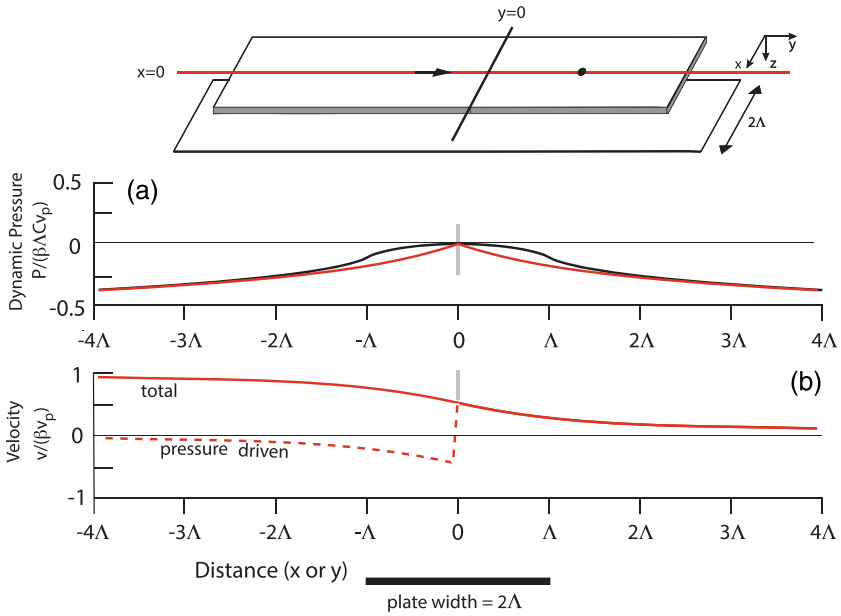

Figure 5. (top) Profiles (red and black lines) through a convergent boundary with no slab; black line is also the plate boundary. The left plate velocity is v_p, and the right plate velocity is zero. (a) Normalized dynamic pressure, color coded to profile. (b) Total vertically averaged velocity (solid red line) and pressure-driven component of velocity (dashed red line) along midline (red) profile in the top panel.

boundaries because the divergence of the plate velocity is zero across transform boundaries.) To this, we must add an expression for plate-driven flow. The y component (trench-normal) of the resulting velocity, evaluated along the y axis, is

$$\bar{v}_y(0, y') = A\frac{2}{\pi}\tan^{-1}\left(\frac{1}{y'}\right) + \begin{cases} \beta v_p & y' < 0 \\ \beta v_o & y' > 0 \end{cases}. \tag{18}$$

The first term on the right-hand side is the pressure-driven component of flow, and the second term (after the single curly bracket) is the plate-driven component of flow. Because $\bar{v}_y$ must continuous at the convergent boundary, we find $A = \beta(v_p - v_o)/2$.

This pressure-driven component of asthenospheric velocity depends only on the difference in plate velocity at the convergent plate boundary and is discontinuous across it (Figures 3 and 4). The plate-driven component of velocity depends only on the local plate velocity and so is also discontinuous across the convergent plate boundary. However, the total flow (pressure-driven plus plate-driven) is continuous, as required by volume conservation. The corresponding pressure, evaluated along the y axis, is

$$P(0, y') = (\beta v_o - \beta v_p)(C\Lambda)\left\{\left(\frac{y'}{\pi}\right)\tan^{-1}\left(\frac{1}{y'}\right) + \frac{1}{2\pi}\ln\left(1 + y'^2\right)\right\}. \tag{19}$$

Figure 5 shows the pressure and velocity along the y axis when $v_o = 0$, so that only the one plate moves relative to the base of the asthenosphere. Pressure scales linearly with $\beta v_p C\Lambda$, and the velocity scales linearly with βv_p. Therefore, the magnitude of the pressure scales with the length of the convergent boundary, 2Λ, but the magnitude of velocity does not. (Note that the length scaling of the solution depends linearly on Λ and does not depend on the asthenospheric thickness or the nature of the surface or basal boundary conditions.) For uniform viscosity, the vertically averaged velocity for the fixed velocity base ($\beta = 1/2$) is half that for the stress-free base ($\beta = 1$). Conversely, the pressure and pressure gradients for the fixed velocity base ($\beta C = 2$) are twice that for the stress-free base ($\beta C = 1$) (Equations 16–19).

4.1.2. Paired Convergent-Divergent Plate Boundaries Without Slab

We now add a divergent plate boundary at $y' = -d'$ so that there is a "middle" plate covering the domain $|x'| < 1, d' < y' < 0$ with velocity $v_p\hat{\boldsymbol{y}}$. The other, stationary, plate occupies the rest of the x-y plane (Figure 6). Proceeding as before, we use two P_{edge} functions, one centered above each nontransform boundary. Evaluating the coefficients of the P_{edge} functions to provide continuity of flow across the boundaries yields

$$\bar{v}_y(0, y') = \frac{\beta v_p}{\pi}\left[\tan^{-1}\left(\frac{1}{y'}\right) - \tan^{-1}\left(\frac{1}{y' + d'}\right)\right] + \begin{cases} \beta v_p & (-d' < y' < 0) \\ 0 & \text{elsewhere} \end{cases}, \tag{20}$$

$$P(0, y') = C\Lambda\frac{v_p\beta}{\pi}\left\{(y' + d')\tan^{-1}\left(\frac{1}{y' + d'}\right) + \frac{1}{2}\ln\left[1 + (y' + d')^2\right]\right\} - C\Lambda\frac{v_p\beta}{\pi}\left\{y'\tan^{-1}\left(\frac{1}{y'}\right) + \frac{1}{2}\ln\left(1 + y'^2\right)\right\}. \tag{21}$$

This solution shows how pressure and velocity depend on the dimensions of the middle plate. If the plate aspect ratio, $d' = (d/\Lambda)$, is small compared to one, so that the plate is short compared to the trench length, the vertically averaged velocity is approximately βv_p beneath the middle plate and zero everywhere else. If d' is large compared to one, the vertically averaged velocity tends toward a limit of $\beta v_p/2$ adjacent to the convergent and divergent boundary and βv_p only midway between the plate

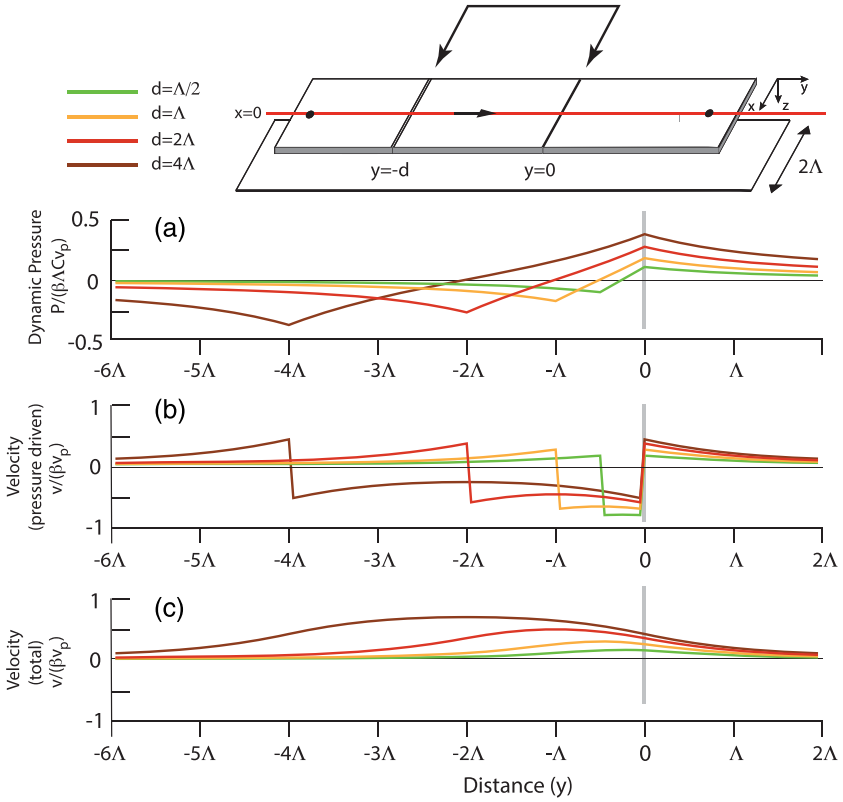

Figure 6. (top) Profile through paired divergent-convergent boundaries, with no slab. (a) Normalized dynamic pressure. (b) Pressure-driven component of vertically averaged velocity. (c) Total vertically averaged velocity. Plate width (perpendicular to profile) is 2Λ; middle plate lengths vary from $d = \Lambda/2$ to $d = 4\Lambda$. Middle plate velocity is v_p (moving right); other plate velocities are zero.

boundaries. For plate aspect ratios between 0.1 and 10, the change in pressure across the plate (equivalently, the average pressure gradient across the plate times the length of the plate) grows approximately as $\pi\Lambda d'$ for $d' < \sim 2$ and is nearly constant for $d' > \sim 2$.Therefore, the pressure difference scales approximately linearly with the shortest plate dimension.

4.2. Plate Boundaries With Slabs

Pressure and velocity change significantly when a slab wall is inserted at the convergent boundary, forming a barrier to asthenospheric flow. Here, we treat slabs as zero-width vertical barriers (for exploration of the role of finite width slab regions, see sections 5 and 6). We will use the term "slab motion" to mean horizontal motion of this vertical barrier.

4.2.1. Slab Motion Only

We begin with slab motion only, so as to separate the effects of slab motion from those of plate motion. Consider a slab wall extending from $x' = -1$ to $x' = 1$ at $y' = 0$ and having a slab velocity $v_w\hat{\boldsymbol{y}}$ (Figure 7). We solve for asthenospheric pressure and velocity with one function P_{wall} centered at the slab wall and set the slab-normal component of velocity adjacent to the slab equal to that of the slab wall, v_w. Then, $B = v_w$ (Equations 13–15) and, evaluated along the y axis:

$$P(0, y') = v_w C\Lambda \left[y' \left(\frac{y'^2 + 1}{y'^2} \right)^{1/2} - y' \right], \tag{22}$$

$$v_y(0, y') = v_w \left[1 - \left(\frac{y'^2}{y'^2 + 1} \right)^{1/2} \right] \tag{23}$$

(Figures 3b and 7). Along the x axis, the pressure discontinuity across the slab is

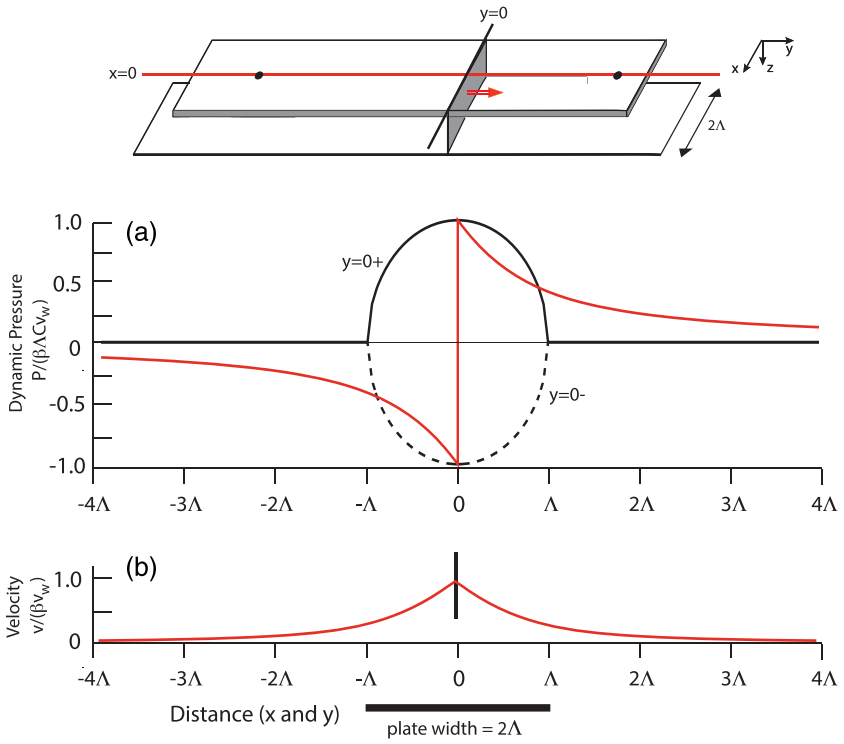

Figure 7. (top) Profiles (red and black lines) through a slab moving to the right with velocity v_w. (a) Normalized dynamic pressure, color coded to profile (solid black line is pressure on the right side of slab; dashed black line is pressure on the left side of slab). (b) Total vertically averaged velocity along midline (red) profile in the top panel.

$$\Delta P_{\text{slab}}\left(x'\right) = 2v_w C\Lambda\sqrt{1-x'^2}. \tag{24}$$

The pressure and the pressure discontinuity across the slab scale linearly with slab length (2Λ). For uniform viscosity, the magnitude of the pressure discontinuity and the pressure gradient near the slab is 4 times larger for the fixed velocity base than for the stress-free base. This can be compared to the responses of the pressure gradient to plate motion, which differ only by a factor of 2 for the differing basal boundary conditions.

4.2.2. Slab and Plate Motion Combined

Starting with the solution for asthenospheric velocities without a slab barrier at the convergent boundary (section 4.1.2 and Equations 20 and 21), we add a function of form P_{wall} centered above the slab wall and solve for B by requiring the velocity of the asthenosphere adjacent to either side of the slab wall to be v_w. Evaluating adjacent to the slab wall ($y' = 0$ and $|x'| < 1$) yields

$$v_w = -\frac{\beta v_p}{2\pi}\left[\tan^{-1}\left(\frac{x'+1}{d'}\right) - \tan^{-1}\left(\frac{x'-1}{d'}\right)\right] + \frac{\beta v_p}{2} + B. \tag{25}$$

Because B must be a constant, this equation does not have a solution because the term in square brackets depends on x. In order to obtain a solution that is accurate everywhere, the slab boundary should be divided into multiple segments and P_{wall} determined for each segment (see section 6). However, we obtain a very good approximate result, which is useful for conceptual understanding, by evaluating the velocity in the center of the slab ($x' = 0$):

$$B = v_w - \frac{\beta v_p}{\pi}\tan^{-1}\left(d'\right). \tag{26}$$

This yields expressions for velocity and pressure along the y axis given in Equations (20) and (21), with the addition of the P_{wall} solution generated by the slab wall:

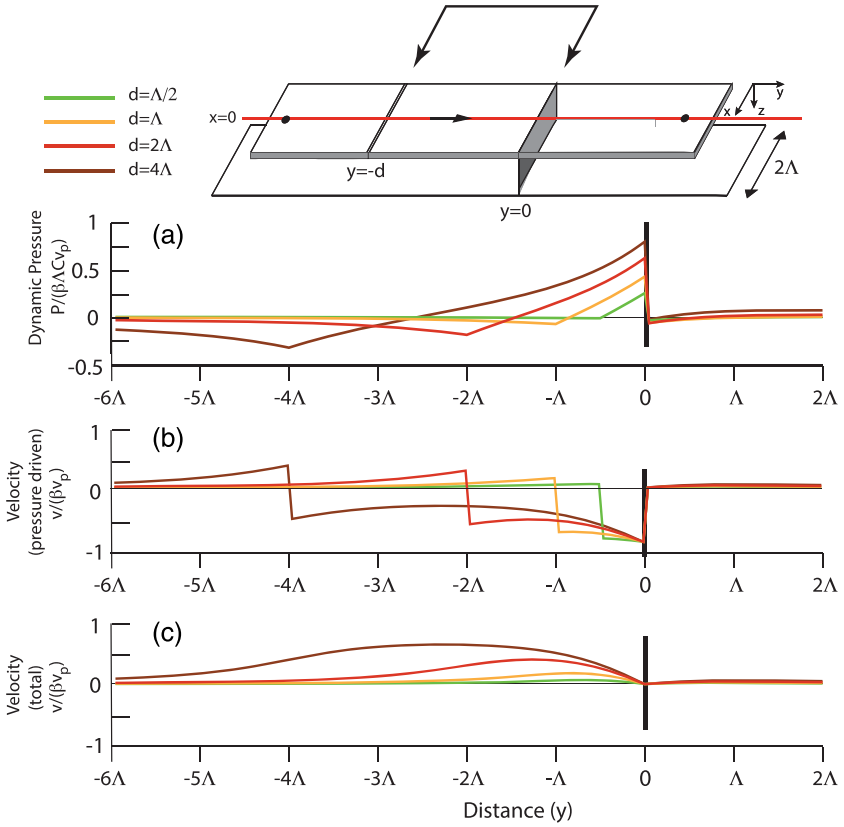

Figure 8. (top) Profile through paired divergent-convergent boundaries, with a stationary slab wall at the convergent boundary. (a) Normalized dynamic pressure. (b) Pressure-driven component of vertically averaged velocity. (c) Total vertically averaged velocity. Middle plate lengths vary from $d = \Lambda/2$ to $d = 4\Lambda$. Middle plate moves right at velocity v_p; other plates are stationary.

$$\bar{v}_y(0,y')_{\text{slab}} = \bar{v}_y(0,y')_{\text{no slab}} + \left(v_w - \frac{\beta v_p}{\pi}\tan^{-1}(d')\right)\left[1 - \left(\frac{y'^2}{y'^2+1}\right)^{1/2}\right], \tag{27}$$

$$P(0,y')_{\text{slab}} = P(0,y')_{\text{no slab}} + C\Lambda\left(v_w - \frac{\beta v_p}{\pi}\tan^{-1}(d')\right)y'\left[\left(\frac{y'^2+1}{y'^2}\right)^{1/2} - 1\right]. \tag{28}$$

The discontinuity in pressure across the slab is

$$\Delta P_{\text{slab}} = 2C\Lambda\left(v_w - \frac{\beta v_p}{\pi}\tan^{-1}(d')\right)\sqrt{1-x'^2}. \tag{29}$$

When $v_w = 0$, the slab wall is stationary relative to the stationary right plate (Figure 8) and the geometry is a (left) plate subducting at the slab wall with velocity v_p. In this case, the pressure is positive beneath the subducting plate, with pressure decreasing away from the slab wall. The pressure-driven component of asthenospheric flow is away from the slab wall, counterbalancing the plate-driven component of flow, which is toward the slab wall. The asthenospheric velocity beneath the overriding (right) plate is near zero because the velocity of the plate, the slab wall, and the base of the asthenosphere is equal. This demonstrates an important general principle: Changes in plate velocity and geometry that occur on one side of a slab wall have little effect on the velocity or pressure on the other side of the slab wall.

The contribution of the subducting plate to the pressure discontinuity depends on both the aspect ratio, d', and width, 2Λ, of the downgoing plate. For $d' \gg 1$, the pressure discontinuity scales linearly with $\beta v_p \Lambda$; for d

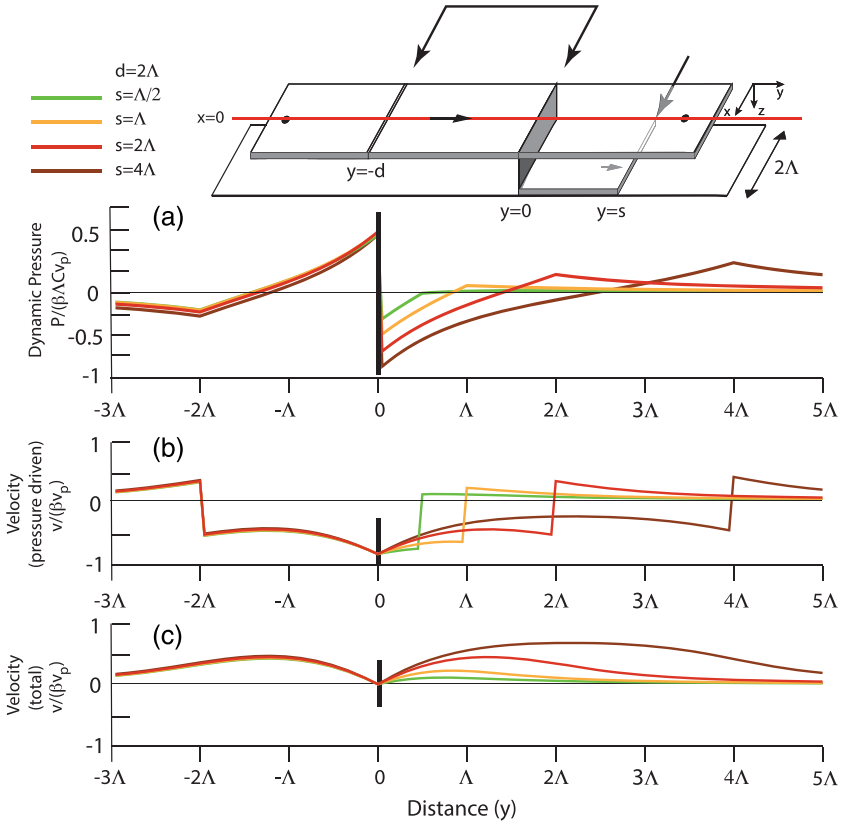

Figure 9. (top) Profile through paired divergent-convergent boundaries, with a stationary slab wall at the convergent boundary and a slab tail to its right. (a) Normalized dynamic pressure. (b) Pressure-driven component of vertically averaged velocity. (c) Total vertically averaged velocity. Middle plate length is 2Λ; slab tail lengths vary from $s = \Lambda/2$ to $d = 4\Lambda$. Middle plate and slab tail move right at velocity v_p; other plates are stationary.

$' \ll 1$, it scales as $(\beta v_p)(2d'\Lambda/\pi)$; and for $d' \approx 2$, an equidimensional subducting plate, it is approximately $(\beta v_p)(2\Lambda/\pi)$. Therefore, the magnitude of the pressure discontinuity scales with the shortest plate dimension.

4.2.3. Slab Flattened Onto the Base of the Upper Mantle

Some subduction boundaries, notably along the northwestern Pacific plate margin at the latitude of Japan, display a "slab tail" where the slab flattens onto the base of the upper mantle (with or without eventual penetration into the lower mantle). For the purpose of illustration, we use the same geometry as above (section 4.2.2) and add a "slab tail" moving to the right along the base of the upper mantle with velocity $v_p\hat{\boldsymbol{y}}$. The slab tail has boundaries at $x' = \pm 1$, $y' = 0$, and $y' = s'$ (Figure 9). For the fixed velocity base, pressure and velocity can be determined using the same approach as before, requiring continuity of vertically integrated velocity at all plate boundaries and at the end of the slab tail, at $y' = s'$.

For all scenarios where the base of the asthenosphere overlying the slab tail is required to have the same velocity as the slab tail, a low-pressure region develops above the slab tail and increases the pressure difference across the slab (Figure 9). Above the slab tail, pressure is most negative adjacent to the slab wall and increases to more positive values away from the slab wall. This means that the pressure-driven component of asthenospheric flow beneath the overriding plate is toward the slab wall, counterbalancing the component of plate-driven flow induced by the slab tail moving away from the slab wall.

In cases where the asthenosphere has a stress-free base everywhere except above the slab tail, and above the slab tail its velocity is set equal to that of the slab tail, computation of the resulting pressures and velocities is complex. In this case, the asthenosphere above the slab tail will have different values of C and β than elsewhere and all boundaries surrounding the slab tail should be divided into multiple small segments and the resulting pressure field computed through a multisegment approach (see section 6). However,

intuition suggests that the plate and slab tail velocities should have a greater effect on pressure in the asthenosphere above the slab tail because βC is larger by a factor of 2 above the slab tail than elsewhere. Results of the multi-segment models presented in section 6 show that this is approximately correct. (See section SB for results for slab tail overturned at the base of the upper mantle.)

4.3. Plate Systems With Two Closely Parallel Slabs

The same general analysis can be used to solve for plate systems with more than one slab. The possible combinations of slab spacing, plate geometry, and velocity are enormous, so in this section, we address two questions: (i) What are the pressure and asthenospheric velocity fields for two closely spaced slabs if all plates are stationary? (ii) At what separation distance do slabs feel the effects of one another via flow induced in the asthenosphere? The second question aims to derive an analytical complement to recent numerical modeling efforts on this topic of slab interaction (e.g., Király et al., 2016, 2018).

Consider a subduction system consisting of two parallel slabs, separated by a distance $2c'$, where $c' = c/\Lambda$, and located at $y' = \pm c', |x'| < 1$. Suppose that the slab profiles move toward each other with velocities $\pm v_w$. Taking advantage of symmetry, we write the velocity of the asthenosphere induced by the motion of the slab profiles as the sum of two P_{wall} solutions and evaluate along the y axis:

$$\bar{v}_y(0, y') = B\left(\frac{|y' - c'|}{\sqrt{1+(y' - c')^2}} - 1\right) + B\left(1 - \frac{|y' + c'|}{\sqrt{1+(y' + c')^2}}\right). \tag{30}$$

Solving for B yields

$$B = v_w\left(1 + \frac{1}{4c'^2}\right)^{1/2}. \tag{31}$$

This shows that the effect of a second slab begins to be felt, at about the 10% level, when $c' \approx 1$, and the separation between slabs is approximately equal to trench length. For very closely spaced slabs, $c' \ll 2$, B increases inversely with slab separation, $B \approx v_w/2c'$, becoming very large when slabs are much closer than the length of the trenches. Computing the resulting dynamic pressure between the slab walls and approximating for $c' \ll 2$ yield

$$P(0, y') \approx C\Lambda v_w \frac{1}{c'}\left(1 + \frac{y'^2 + 5c'^2}{2}\right). \tag{32}$$

Therefore, for small slab separations, $P(0,y') \approx C\Lambda v_w/c'$,and the dynamic pressure between the slabs grows approximately linearly with the inverse of the slab separation. This can become very large when the slab separation is small (Figure 10; see also results for double slab systems in sections 6 and SG). For small slab separations, the y component (slab-normal component) of asthenospheric velocity is near zero between the slabs and convergence between the slabs is accommodated by large slab-parallel velocities between the slabs. Figure 10 also shows that the pressure on the outer side of the slabs (i.e., beneath the leftmost and rightmost plates) does not change significantly as the distance between slabs decreases, again illustrating that pressure (and velocity) on one side of a slab is not affected significantly by processes on the other side of the slab.

4.4. Asthenospheric Flux Into the Lower Mantle at Slab Boundaries

The analytical method described here is generally designed to quantify flow within the upper mantle. However, slabs commonly penetrate the lower mantle (e.g., Fukao & Obayashi, 2013; van der Hilst et al., 1997) and may also facilitate flow of adjacent asthenosphere into the lower mantle. Flow of material out of the upper mantle and into the lower mantle, or vice versa, can be simulated by choosing P_{edge} solutions that do not conserve upper mantle material. For example, flux of asthenosphere into the lower mantle along with the slab can be simulated by adding a net sink along the trench.

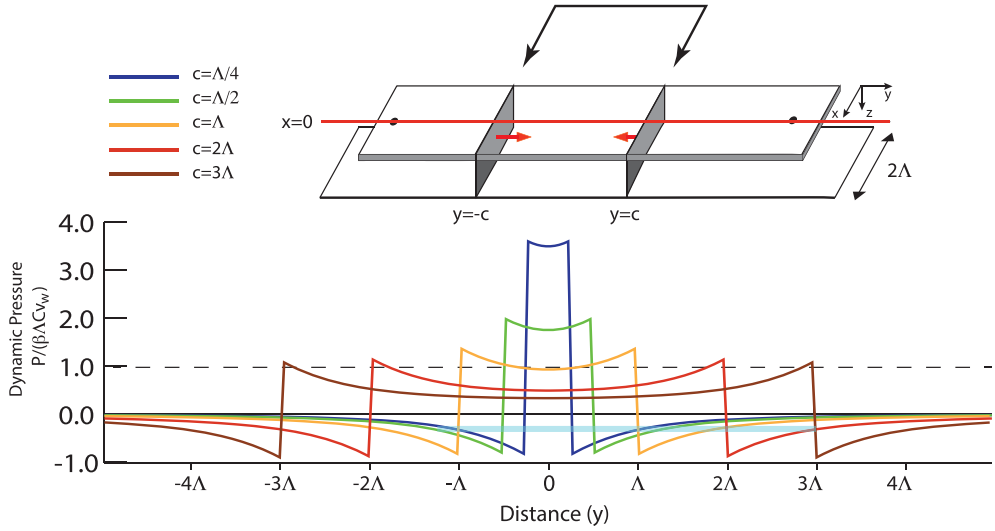

Figure 10. (top) Profile through two converging slab walls, with velocities $\pm v_w$. Half distance between the walls slab varies from $c = \Lambda/4$ to $c = 3\Lambda$. All plates are stationary.

This can be quantified beginning with Equation (20) (with $v_w = 0$) and adding to it a P_{edge} and P_{wall} function centered at the slab wall. In section 4.2.2, we solved for the modifying coefficients, A and B, such that the velocity of the asthenosphere adjacent to the slab wall was constrained to be equal to that of the slab wall (in that case, the value of A was zero.) We now solve for new values of A and B such that there is a net loss of asthenosphere at the slab wall, potentially occurring on either or both sides of the wall. Let $F_{DG} = v_{DG}a_{DG}$ be the flux of asthenosphere into the lower mantle along the downgoing plate side of the slab (where v_{DG} is the velocity of the downfluxing material as it leaves the upper mantle and a_{DG} is its thickness in cross section, referred to in Holt & Royden, 2020, as the flux width). Similarly, let $F_{OR} = v_{OR}a_{OR}$ be the flux of asthenosphere into the lower mantle along the overriding plate side of the slab. Then, we write the resulting equation for velocity, including the as-yet-to-be-determined coefficients A and B, and evaluate on both sides of the slab:

$$\begin{cases} v_w + \dfrac{F_{DG}}{a} = \dfrac{\beta v_p}{\pi}\tan^{-1}\left(\dfrac{1}{d'}\right) + B - A + \eta v_p & y' = 0_- \\ v_w - \dfrac{F_{OR}}{a} = \dfrac{\beta v_p}{\pi}\tan^{-1}\left(\dfrac{1}{d'}\right) + B + A & y' = 0_+ \end{cases} \tag{33}$$

Yielding:

$$\begin{cases} B = v_w - \dfrac{\beta v_p}{\pi}\tan^{-1}(d') + \left[\dfrac{F_{DG} - F_{OR}}{2a}\right] \\ A = \dfrac{\beta v_p}{2} - \left[\dfrac{F_{DG} + F_{OR}}{2a}\right] \end{cases} \tag{34}$$

where the terms in square brackets represent the effects of asthenospheric flux into the lower mantle. Figures 11 and 12 show the resulting dynamic pressure for a stationary slab ($v_w = 0$).

As the total material fluxed into the lower mantle increases, A becomes more negative. If the material is fluxed into the lower mantle on the downgoing plate side of the slab (Figure 11, $F_{OR} = 0$), B becomes less negative and the pressure discontinuity across the slab wall becomes less. If the material is fluxed into the lower mantle on the overriding plate side of the slab (Figure 12, $F_{DG} = 0$), B becomes more negative and the pressure discontinuity across the slab wall increases. (Because the asthenospheric channel extends to

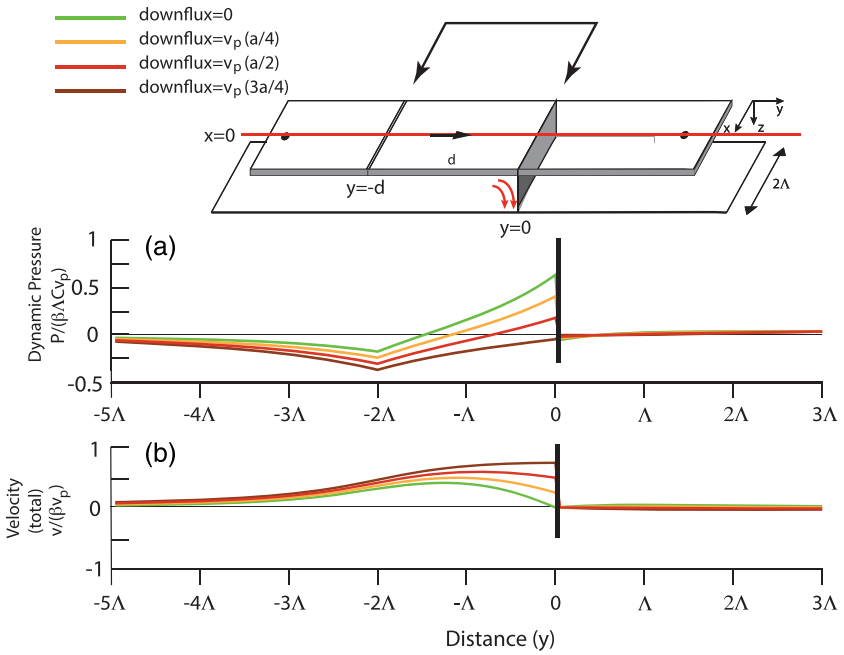

Figure 11. (top): Asthenosphere beneath a subducting (left) plate moves into the lower mantle at the slab wall (red arrows) along profile through paired divergent-convergent boundaries, with a stationary slab wall at the convergent boundary. (a) Normalized dynamic pressure. (b) Pressure-driven component of vertically averaged velocity. (c) Total vertically averaged velocity. Middle plate moves right at velocity v_p; other plates are stationary.

infinity in these Cartesian models, unlike the geometry for a sphere, no counterbalancing flux is needed from lower mantle to upper mantle.)

5. Assessment and Limitations of the Hele-Shaw Approximation

The Hele-Shaw approach to calculating linear viscous flow in a thin channel is advantageous for ease and speed of computation; it reduces 3-D viscous flow to a 2-D computation and relies on solving a second-order partial differential equation for pressure in 2-D rather than fourth-order partial differential equations for coupled stream functions in 3-D. The main inaccuracy of the Hele-Shaw method is that, because shear stresses on vertical planes are neglected, only boundary-normal velocities can be constrained at boundaries to the flow, including boundaries where there are obstructions to flow such as at slab walls. We can gain insight into the inaccuracies resulting from the Hele-Shaw approximation to flow, and develop a compensatory strategy, through comparison to more complete solutions for channel flow.

5.1. Assessing (and Improving) the Hele-Shaw Approximation

A geometry that lends itself to more exact solutions consists of a semi-infinite channel bounded by a linear wall of infinite extent. We consider flow that is confined to a channel, of depth a, that is of infinite extent in the x direction, semi-infinite extent in the y direction ($y > 0$), and has an infinite vertical boundary at $y = 0$ (extending to $x = \pm\infty$). A uniform velocity, $\boldsymbol{v_p}$, is imposed at upper surface of the channel (at $z = 0$), and velocity is set to zero at the base of the channel (at $z = a$).

In a first example, we set the velocity at the top of the channel to be parallel to the wall ($\boldsymbol{v_p} = v_{px}\hat{\boldsymbol{x}}$) and the velocity at the wall to be zero at all depths (Figure 13a). With these constraints, flow in the channel occurs only in the x direction. Comparing the exact solution for vertically averaged velocity (derived in section SC) with the Hele-Shaw result shows that the two solutions do not agree within a boundary layer near the wall, as expected, but are effectively equal for $y \geq a$ (Figure 13b). Most relevant is how this affects the volume rate of flux around obstructions to flow within the channel.

We define boundary-parallel flux as the volume rate of flow between a point located on wall and some point located at distance y from the wall. Figure 13c shows that if boundary-parallel flux is computed by the

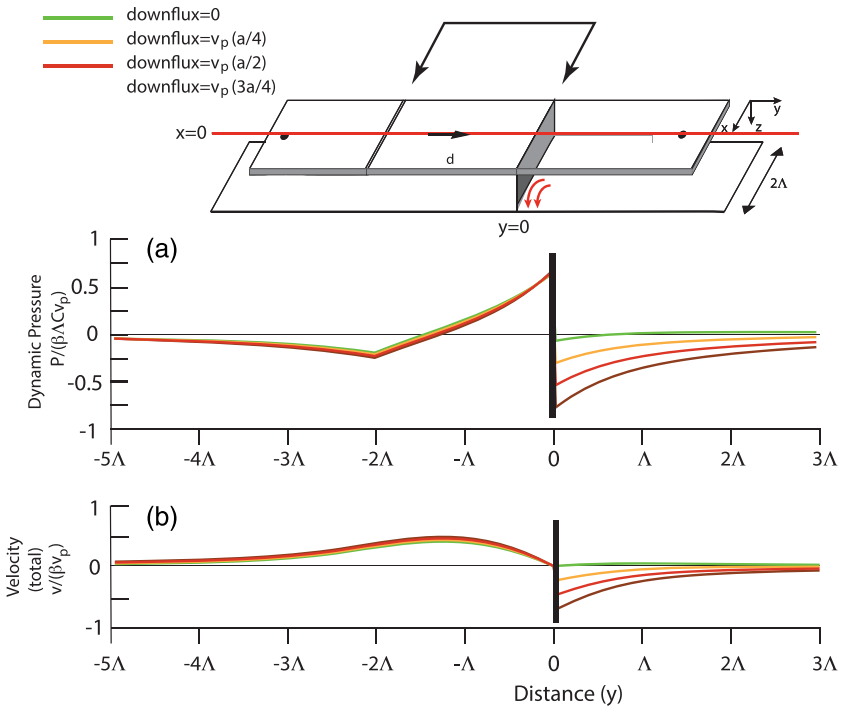

Figure 12. (top) Asthenosphere beneath the overriding (right) plate moves into the lower mantle at the slab wall (red arrows) along profile through paired divergent-convergent boundaries, with a stationary slab wall at the convergent boundary. Asthenosphere beneath the overriding right plate moves into the lower mantle at the slab wall (red arrows) (a) Normalized dynamic pressure. (b) Pressure-driven component of vertically averaged velocity. (c) Total vertically averaged velocity. Middle plate moves right at velocity v_p; other plates are stationary.

Hele-Shaw method for a "padded" wall, that is, one that shifted outward into the flow domain by a distance $a/3$, the "shifted" Hele-Shaw result matches the exact solution for $y \geq a$ (see Equations SC16–SC19 for a mathematical analysis).

We can test whether this result is generally useful by choosing a configuration for flow in a semi-infinite channel that is generally comparable in scaling to the problem of flow around a slab wall of length 2Λ. At the slab wall, we set the boundary-parallel component of velocity to zero and the boundary-normal component of velocity at the wall to be alternately zero and v_p, alternating along segments of length 2Λ (Figure 14a). We prescribe a uniform velocity on the upper surface of the channel that is orthogonal to the wall, ($\boldsymbol{v_p} = v_{py}\hat{\boldsymbol{y}}$), and a velocity of zero at the channel base. We derive a "complete" solution for this geometry that constrains the vertically averaged velocity at the wall in both boundary-normal and boundary-parallel components (section SC). (Comparison between "complete" and exact solutions for the pure shear geometry of Figure 13a is shown in Figure 13b, indicating that constraining only the vertically averaged shear flow at the boundary gives reasonably accurate results.)

"Complete" solutions for vertically averaged velocities ($\overline{v}_x, \overline{v}_y$,) and dynamic pressure are shown for $\Lambda = a$ to $\Lambda = 8a$ in Figure 14. The dynamic pressure and boundary-normal velocities are shown along profiles corresponding to $x = \Lambda$, passing through the center of a zero-velocity wall segment. The boundary-parallel velocities are shown along profiles corresponding to $x = \Lambda/2$ (boundary-parallel velocity is zero at $x = \Lambda$). Also shown are Hele-Shaw solutions for the same geometry, but computed for a "padded" wall, that is shifted outward into the flow domain by a distance of $a/3$.

Figures 14b and 14c show that the "shifted" Hele-Shaw solutions for vertically averaged flow are effectively equal to those of the complete solution outside of a narrow boundary layer. The width of the boundary layer is approximately $3a/2$ for boundary-parallel flow and $3a/4$ for boundary-normal flow. The pressures computed by the two methods are effectively equal everywhere. This indicates that padding of boundaries around obstructions to flow by a distance equal to one third of the channel depth effectively corrects for the inability of the Hele-Shaw method to constrain boundary-parallel velocities.

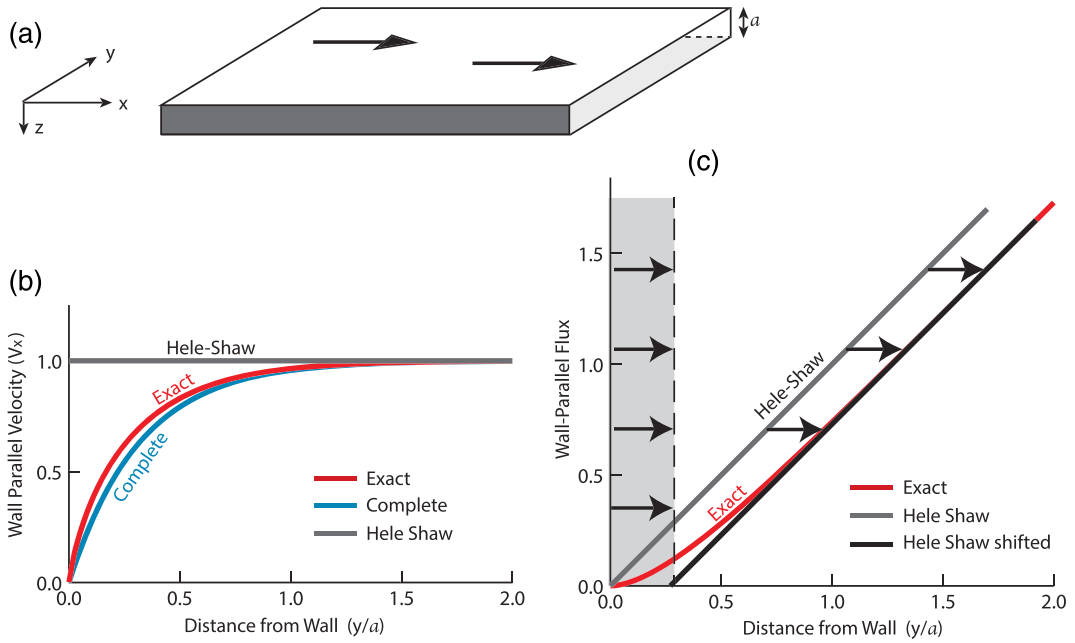

Figure 13. (a) Block diagram for channel flow in a semi-infinite half space with infinite vertical wall at $y = 0$ and zero-velocity boundary condition imposed at the wall. (b) Vertically averaged velocity computed by exact, "complete," and Hele-Shaw methods. (c) Wall-parallel volume flux computed by exact and Hele-Shaw methods and by Hele-Shaw method for a padded wall, shifted to the right as shown by shading and arrows.

Dynamic pressure for the shifted Hele-Shaw solutions can be extrapolated into the domain $y < a/3$ using a Hele-Shaw solution that sets the boundary-normal velocity equal to zero in this domain, or

$$\bar{v}_x = 0 = -\frac{\partial P}{\partial x}\left(\frac{a^2}{12\mu}\right) + \frac{v_p}{2}. \tag{35}$$

Figure 14d shows that dynamic pressures extrapolated to $y = 0$ using this strategy are in excellent agreement with those from the full solution.

The results shown in Figures 13 and 14 suggest a strategy to compensate for the main shortcoming of Hele-Shaw solutions: All the boundaries that define obstructions to flow should be shifted outward, or padded, by one third of the channel depth (see sections 6 and SE). Results in Figure 14 also demonstrate that inaccuracies in the unshifted Hele-Shaw solutions scale with channel depth (a) and not with the length of the barrier to flow (2Λ). Because the magnitude of dynamic pressure scales approximately linearly with Λ, padding of boundaries is proportionally important when (Λ/a) is small. Padding is also important when barriers to flow are separated by distances that are small compared to the channel depth, such as for closely spaced slabs (section 6.2.2). Padding is much less important when (Λ/a) is large, for example, greater than about 8.

In Figure 14d, small differences in the Hele-Shaw and full solutions for dynamic pressure just begin to be apparent for $\Lambda = \alpha$, indicating that the Hele-Shaw method will not produce accurate results for obstructions that are much smaller than twice the channel depth. The Hele-Shaw method is also not applicable to channel flow where there are free-slip boundary conditions on both the upper and lower boundaries of the channel, in which case deviatoric stresses control the flow geometry.

5.2. Assessing Effects of Depth-Dependent Viscosity

Although we have not benchmarked our analytical method against numerical solutions for depth-dependent viscosities through the upper mantle, the method is expected to be comparably accurate for depth-dependent and uniform viscosity layers. In the Earth, the lower part of the upper mantle is generally thought to have a viscosity several times greater than that of the upper (sublithospheric), seismically

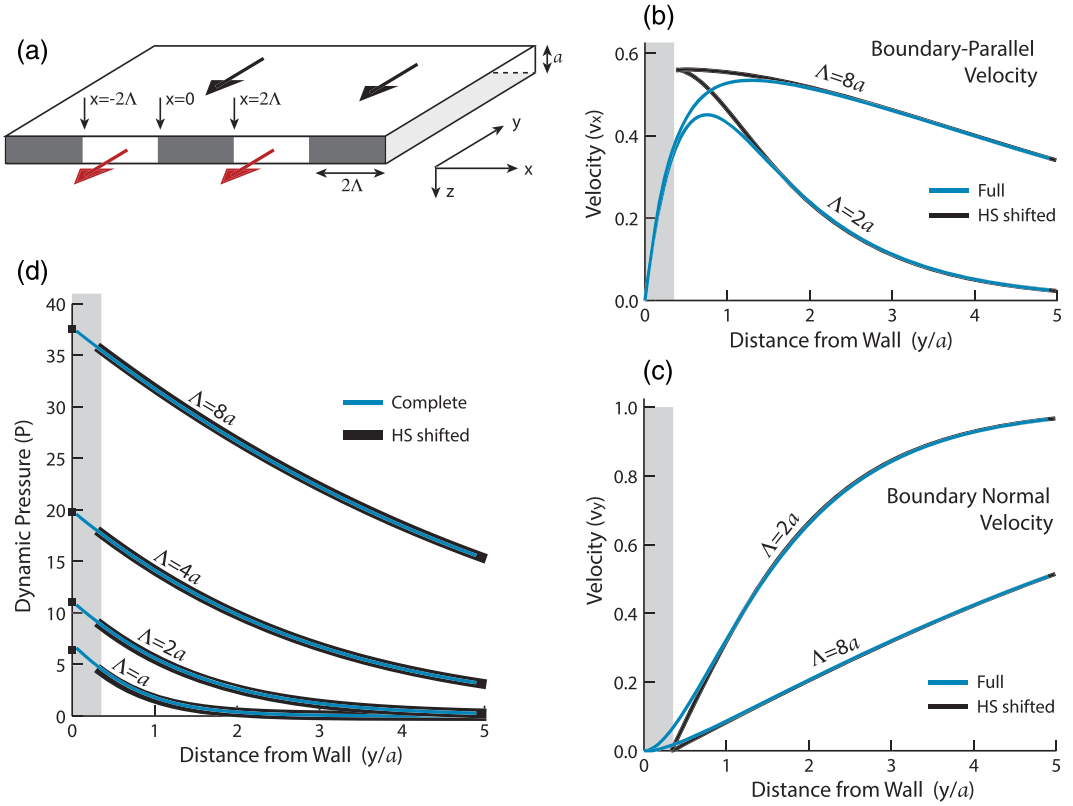

Figure 14. (a) Block diagram for channel flow in a semi-infinite half space. Velocity boundary conditions at $y = 0$ are $v_x = 0$ and periodic wall-normal velocity: $v_y = 0$ $(-2\Lambda \le x \le 0)$, $y_x = 2v_p$ $(0 \le x \le 2\Lambda)$. (b) Vertically averaged wall-parallel velocity along $x = \Lambda/2$. (c) Vertically averaged wall-normal velocity along $x = \Lambda$. (d) Normalized dynamic pressure along $x = \Lambda$. Results are computed by a "complete" method described in the text and by a shifted Hele-Shaw method with velocity boundary conditions applied at $y = a/3$. Black dots show extrapolation of Hele-Shaw pressure to $y = 0$.

slow part of the upper mantle (e.g., Gutenberg, 1959; Richards et al., 2001). The general effect of such a viscosity distribution can be demonstrated by considering a simplified case where the plates move relative to a fixed velocity base, with the thickness of the lithosphere set to zero and the upper mantle divided into two equally thick layers, with viscosity $\mu = \mu_o$ in the upper layer and viscosity $\mu = R\mu_o$ in the lower layer.

Equation (8) shows that scaling of the component of the dynamic pressure field arising from the (trench-normal) slab velocities is proportional to the viscosity coefficient C, while scaling of that component of the dynamic pressure field arising from the plate velocities is proportional to the product of the viscosity coefficient and the coupling coefficient, $C\beta$ (C and β defined in Equations 6 and 7) Computing C and β for this two-layer upper mantle, with equal layer thickness, gives

$$C = C_o\left[\frac{8R(1+R)}{(1+R)^2 + 12R}\right] \qquad \beta = \beta_o\left(\frac{R+3}{2+2R}\right), \tag{36}$$

where C_o and β_o are the viscosity and coupling coefficients for an upper mantle with uniform viscosity μ_o (i.e., $R = 1$).

If, for example, the viscosity of the lower layer is 4 times greater than that of the upper layer ($R = 4$), then $C = 2.19\ C_o$ and $C\beta = 1.53\ C_o\beta_o$. This means that, for the two-layer model, the response of the dynamic pressure field to the imposed plate velocities will be identical to the response of a uniform viscosity upper mantle with $\mu = 1.53\ \mu_o$. In contrast, the response of the dynamic pressure field to the imposed slab velocities will be approximately 40% greater than the response of a uniform viscosity upper mantle with $\mu = 1.53\ \mu_o$.

Because down-flux of asthenosphere adjacent to the slabs can be parameterized as adjustment to the wall velocity on one (or both) sides of the slab (section 4.4), the response of the dynamic pressure field to down-flux adjacent to the slab will also be ~40% greater for a stratified mantle ($R = 4$) than for a uniform viscosity mantle with $\mu = 1.53\ \mu_o$. This is particularly relevant for our application of this method to real Earth geometries (Holt & Royden, 2020), because a smaller rate of down-flux (or smaller flux width) will be needed to achieve the same effect on the dynamic pressure field. In the case where $R = 4$, this corresponds to a reduction in down-flux rate by approximately 40%.

Thus, the method presented here is applicable to the dynamic pressure associated with flow in an upper mantle with depth-dependent viscosity. But the relative dependence of dynamic pressure on slab velocity and plate velocity will, for reasonable Earth values, vary somewhat from those computed using a uniform viscosity model, in an easily computed manner. As for the uniform viscosity case, dynamic pressure is uniform as a function of depth, as is important in our application of this method to real Earth geometries (Holt & Royden, 2020).

5.3. General Limitations to the Analytical Method

General limitations of the method we have developed, as pertains to flow in the asthenosphere, is that is does not connect, dynamically, flow in the upper mantle to flow in the lower mantle. While transfer between upper mantle and lower mantle can be prescribed to occur in a specific location, there is no means of determining from the Hele-Shaw method where such exchange of material should occur.

Local effects related to subduction, such as the fact that descending slabs are not vertical and exhibit both vertical and horizontal components of velocity, are not generally significant outside of a narrow region localized around the slab and do not generally extend beyond the "padded" region around the slab wall. Exceptions may occur for very shallowly dipping slabs, where the dipping slab occupies a wider region than is defined by the padding. Our benchmarking results suggest that, in such cases, widening the padded region to enclose the entire dipping portions of the slab is a satisfactory accommodation (Figure SG1). However, the general concept of padding of the region around the slab wall should not be mistaken for the emergence of local effects; padding is a compensation for the main shortcoming of Hele-Shaw flow models, and the approximate padding distance can be derived mathematically.

Hele-Shaw methods are not designed to model nonlinear viscosity. However, the method developed in this paper is able to incorporate lateral variation in viscosity by prescribing domains in which viscosity is laterally invariant and separating them from one another by domain boundaries, treated in the same way as plate boundaries. Alternatively, Equations (9) and (10) can be solved numerically. Although this does not completely preserve the speed of the analytic solution, it still collapses 3-D flows into a 2-D differential equation, resulting in much faster computations than for full 3-D numerical solution.

6. Complex Geometries Defined With Many Boundary Segments

Pressure solutions for complex plate and slab geometries, and/or more accurate solutions for simple geometries, can be obtained by dividing all plate boundaries (and slab tail boundaries) into shorter segments and solving Equations (9) and (10) using a multi-segment adaptation of the method presented here. Our analytic approach computes solutions for systems with more than 1,000 plate boundary segments and arbitrarily large dimensions in several seconds on a reasonably fast laptop computer.

6.1. Analytic Approach to Multi-segment Plate Boundaries

For any arbitrary plate and slab geometry, plate boundaries and slabs can be divided into segments that are short compared to the thickness of the asthenosphere and to the length of the plate boundary. We achieve good results for slab boundaries divided into segment lengths shorter than or equal to about one fifth of the channel depth and segment lengths on non-slab boundaries of about twice that.

If there are N plate boundary segments in the system, we write a function of the form P_{edge} for each plate boundary segment, so that the nth P_{edge} function (which we denote $P_{\text{edge},n}$) is centered about the nth plate boundary (see section 3.2 for discussion of how this is accomplished for arbitrarily located and orientated segments). In the same way, we also write a functions $P_{\text{wall},n}$ for every segment that contains a slab wall.

Each of these functions will be modified by a coefficient, denoted as A_n for the P_{edge} functions and B_n for the P_{wall} functions (see Equations 11 and 13).

The total pressure field then consists of the sum of all of these functions, with the as-yet-to-be-determined coefficients, A_n and B_n. (B_n will be zero for all nonslab boundaries.)

$$P(x, y) = \sum_{n=1}^{N} A_n P_{\text{edge},n} + B_n P_{\text{wall},n}. \tag{37}$$

A_n and B_n are determined by matrix inversion. The constraints on the matrix inversion are that the boundary-normal velocity (averaged over depth and including the plates and slab tails, i.e., Equation 9) be equal on either side of all not slab segments. At segments containing slab walls, the boundary-normal velocity of the asthenosphere on both sides of the slab wall (without plates or slab tails, i.e., Equation 8) is equal to that of the slab wall.

Because the P_{wall} terms produce rapidly varying velocities adjacent to the end of the plate boundary segment about which they are centered, this causes problems if we evaluate the associated velocities at the center of the adjacent segment. To correct for this, we instead evaluate asthenospheric velocities induced by the P_{wall} terms (but not the P_{edge} terms) using the average boundary-normal velocity along each segment rather than the velocity at the segment center (Equations SA15 and SA16).

6.2. Benchmarking for Multi-segment Plate Boundaries

We compare the results of the analytical, multisegment approach to the results of 3-D numerical modeling using a setup and methodology identical to that of Holt et al. (2017). These numerical subduction models employ the finite element code CitcomCU (Moresi & Gurnis 1996; Zhong 2006) to model 3-D, incompressible Stokes flow with a linearly viscous rheology (section SD). We use rectangular plates and consider single and double subduction in a variety of geometries, and normal and overturned slab geometries (i.e., slab dips less than and greater than 90°, respectively). Figure SD1 shows the model setup for the case of a system with a single slab.

For each numerical subduction model, we replicate the geometry in our analytical models, replacing all dipping slabs with vertical walls, co-located with the slab at mid-asthenosphere depth and moving horizontally at the velocity of the slab profile (Figure 2). As per the results of section 5, we pad the sides and ends of the slab wall by 200 km (approximately one third of the asthenospheric thickness). The slab "box" that is 500 km in width (400 km due to padding and an additional 100 km to approximate the thickness of the slab) extends 200 km beyond the edges of the slab (Figure SE1.) We also pad all plate and slab tail edges that abut asthenosphere by 200 km, moving all edges toward the adjacent asthenosphere by 200 km (the former do not occur in nature but are a feature of the numerical models, i.e., Figures 15 and SD1). This padding scheme is applied consistently to all of the model geometries. (The effect of each element in the padding scheme is shown in Figures SE2 and SE3, demonstrating that it is mainly padding of the region around the slab that is important in determining the "correction" to the pressure discontinuity across the slab.)

6.2.1. Single Slab Systems

Figure 15 compares dynamic pressure computed analytically to that computed numerically for two snapshots during progressive subduction of a single slab with trench length of 2,000 km. These "midline" profiles are orthogonal to the trench and pass through its center. Subduction rate, shown on each panel, is calculated as the difference in plate velocity on either side of the subduction zone.

For reference and to build intuition, Figure 15 contains cross sections, extracted from the numerical results, of pressure and velocity as a function of depth, with the region of the slab box also shown on the cross section. These show that outside of the slab box, the primary signal in the pressure field is largely depth invariant, consistent with the primary assumption of the Hele-Shaw method. (The shallow regions of high pressure where no plate is present are a product of the surface boundary conditions that substitute pressure for topography in the numerical models). The numerically determined pressures along each profile are taken at mid-asthenospheric depth (330 km) and compared to the analytical results.

The general concepts developed in section 4 are displayed on these profiles. There is positive pressure beneath the subducting slab (downgoing plate side) and negative pressure above the slab (overriding plate side). The slab-normal pressure gradient in the asthenosphere above the slab tail is approximately twice

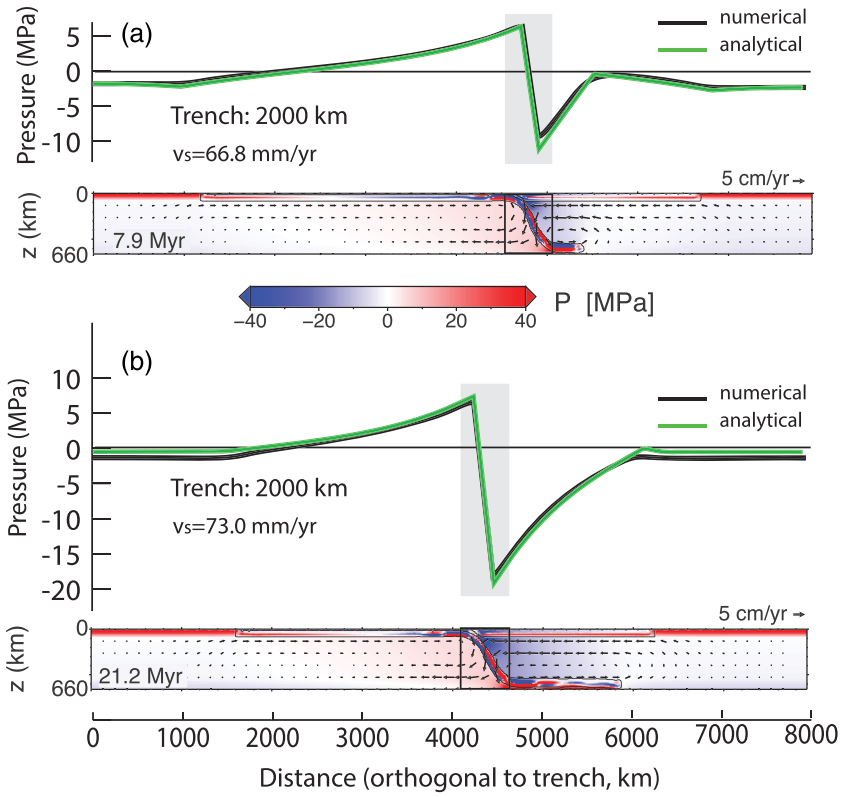

Figure 15. Numerically (black line) and analytically (green lines) determined dynamic pressure along midline trench-perpendicular profiles through a single slab system undergoing progressive subduction. v_s is subduction velocity determined as the difference in plate velocity on either side of the trench. Cross sections of numerically determined dynamic pressure (color shading) and asthenospheric velocity (arrows) are shown below each profile. Gray regions on pressure profiles and black outlines on cross sections indicate the extent of the slab box.

the slab-normal pressure gradient in the asthenosphere below the subducting plate. This occurs because the ratio of pressure gradient to plate (or slab tail) velocity is greater by a factor of 2 where there are both an upper and lower velocity boundary conditions (see Equations 16 and 17). Therefore, the total pressure difference across the slab increases with time, as the subducting plate shrinks and the slab tail grows in length.

Figure16 compares analytically and numerically determined midline pressure profiles for three subduction systems with comparable convergence rates (64 to 75 mm/yr) and similar plate and slab tail lengths, but with trenches that vary from 1,000 to 4,000 km in length. The increasing trench lengths result in increasing pressure differences across the slab that scale approximately with the "padded" slab lengths of 1,400 km (ΔP = 13.6 MPa); 2,400 km (ΔP = 21.7 MPa); and 4,400 km (ΔP = 29.6 MPa) (e.g., Stegman et al., 2006).

For all of the profiles displayed, the analytically and numerically determined pressures agree well and illustrate the utility and accuracy of the analytic method with the padding scheme employed. Trench-parallel profiles located on the overriding plate side of the slab (Figure 16d), at a distance of ~400 km from slab wall, and ~150 km from the padded wall around the slab, illustrate that the analytic method is quite accurate in determining pressure near the sides of the slab box.

The analytic method developed here is aimed at determining dynamic pressure in the asthenosphere as a function of geometry and plate velocity, but it is important to check that the vertically averaged asthenospheric velocities agree generally with those computed numerically. Reproducing velocity is more challenging for the analytic method than reproducing dynamic pressure because, in the analytic approach,

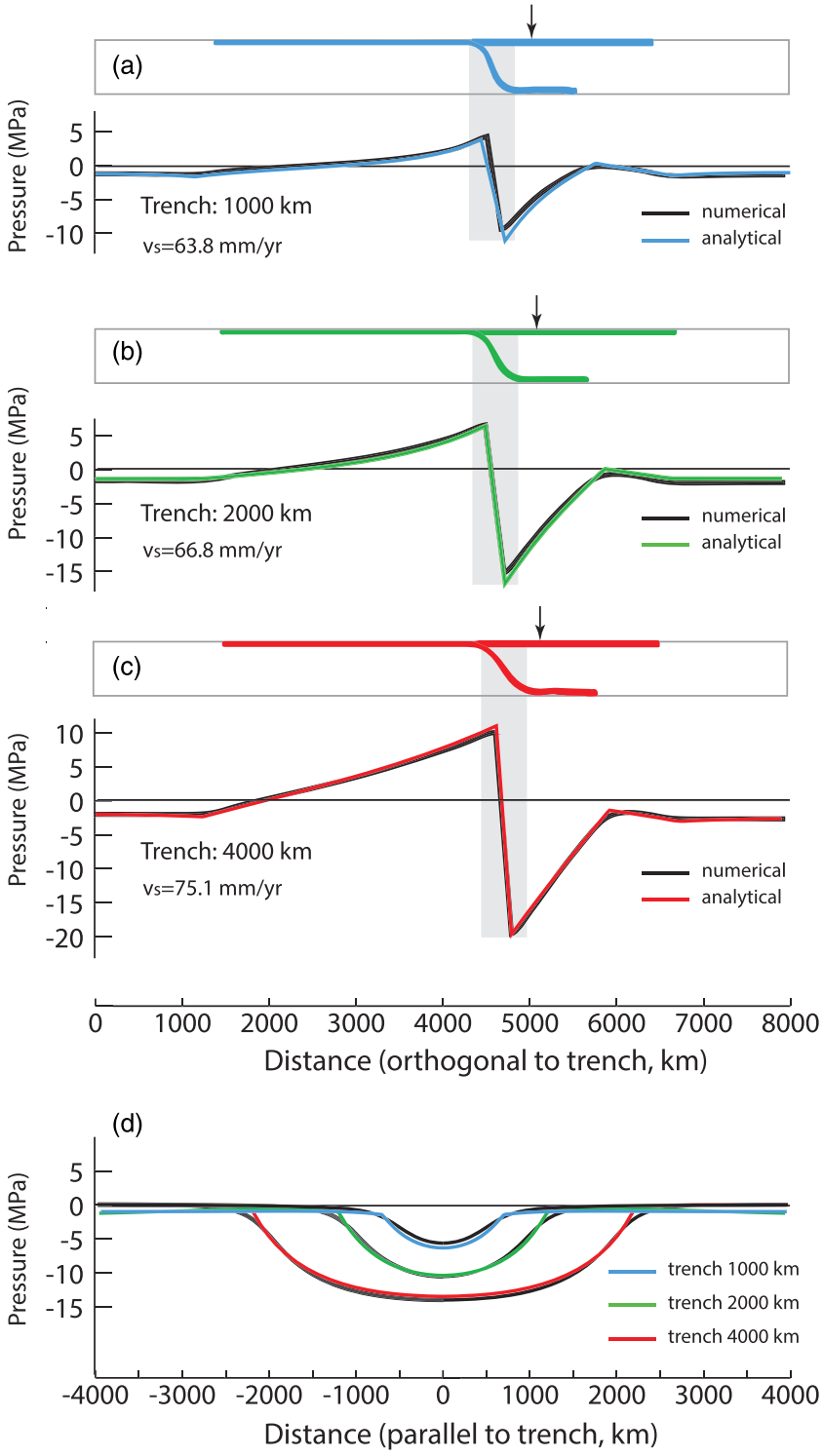

Figure 16. (a-c) Numerically (black line) and analytically (colored lines) determined dynamic pressure along midline trench-perpendicular profiles through a single slab system undergoing progressive subduction (geometry shown above each profile). Gray box indicates padded region around the slab wall. (d) Numerically and analytically determined dynamic preressure along trench-parallel profiles crossing the midline at locations shown by the arrows in panels a-c. v_s is subduction velocity determined as the difference in plate velocity on either side of the trench.

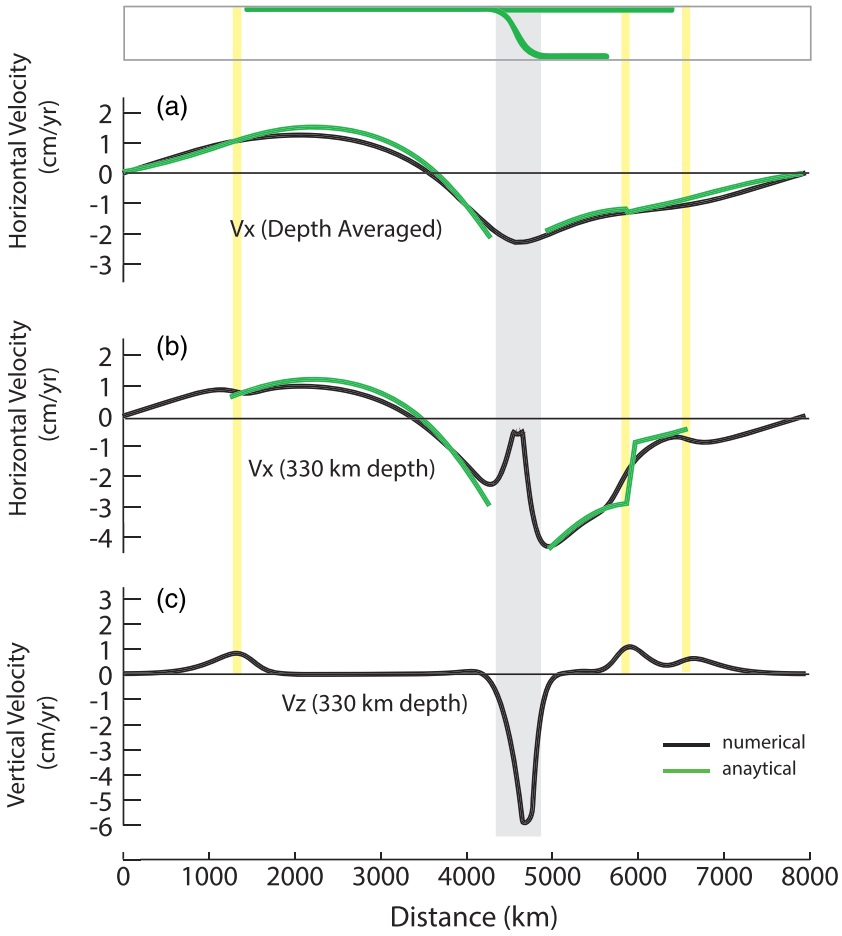

Figure 17. Numerically (black line) and analytically (green lines) determined trench-normal velocities for midline profiles through the single subduction system shown in Figure 16b. (a) Vertically averaged velocities through the upper mantle (plate, asthenosphere, and slab tail); (b) velocity in the asthenosphere at 330 km depth; and (c) vertical velocity computed numerically. Trench length is 2,000 km, and slab geometry is as shown at the top. Gray box indicates slab region, and yellow lines indicate regions with significant vertical velocity in the numerical model.

velocity is computed from horizontal pressure gradients. Therefore, even small errors in pressure can lead to large errors in velocity.

Inspection of the numerically generated cross sections in Figure 15 shows that velocity, as a function of depth, is highly variable. In general, flow is toward the slab in the shallow asthenosphere and away from the slab in the deep asthenosphere. It is the vertical average of the velocity that reflects the total horizontal flux of material. Comparison of numerically computed vertically averaged velocities with those computed analytically captures the extent to which the analytic method correctly reproduces the upper mantle flux.

Vertically averaged velocities for the midline profile of Figure 16b show analytical results that agree reasonably well with the numerical results, although the analytically determined velocities are slightly greater than those numerically determined beneath the downgoing (left) plate (Figure 17). Much of the misfit is probably due to the presence of the unphysical regions of open asthenosphere in the numerical model; the analytical approach treats these regions as if they were overlain by a stationary plate, which affects not only the velocities computed for the regions of open asthenosphere but also those computed beneath the adjacent plates.

The vertical component of the numerically determined velocity (at 330 km depth) is near zero everywhere outside the slab box, except near the edges of the plates and the slab tail (Figure 17c). This is in good agreement with the results from section 5, indicating that velocity should be well fit by a Hele-Shaw approximation, and horizontal, everywhere except near the boundaries of slab walls and plate edges. The vertical

components of velocity can also be seen in the numerically generated cross sections of Figure 15, where they are largely confined to the slab box and regions adjacent to the plate and slab tail edges.

We expect that the analytic method should capture the details of velocity as a function of depth where the flow is essentially horizontal. We can use the velocity at midasthenospheric depth as a proxy for where the analytic method fails to resolve the details of flow at depth. As expected, this occurs near the end of the slab tail, where the numerical results show a significant vertical component in the velocity field. However, within several hundred kilometers on either side of this location, the analytical method accurately resolves the velocity at 330 km depth. (See also velocities on a trench-parallel profile, Figures SF1 and SF2.)

6.2.2. Double Slab Systems

Double subduction systems with closely spaced slabs exhibit a range of behaviors that can differ from those of single subduction systems, presenting an opportunity for additional benchmarking of the Hele-Shaw approach. Here, we show results for three time periods during progressive subduction with symmetrical, double "out-dipping" slabs, with subduction of an intermediate plate along two opposing edges and convergence between the slabs (Figure 18). The magnitude of the dynamic pressure between the converging slabs increases dramatically with decreasing distance between slabs.

In this system, rapid trench-parallel flow must occur between the slabs, as asthenosphere escapes from the narrowing region between slabs. Because of the boundary layer effect for wall-parallel flow, as illustrated in Figure 13b, the effective width over which trench-parallel flow can occur is equal to the separation between slab walls shifted inward by approximately one third of the channel depth. This results in padded values of slab separation, divided by half-trench length, that are approximately 1.0, 0.5, and 0.25. Accordingly, and despite a decrease in slab convergence rate from ~100 to ~75 mm/yr, the pressure between the slabs increases by a factor of 2.5 during progressive subduction. This is consistent with the results of Figure 10, which shows that the pressure between slabs becomes very large as the distance between slabs becomes small compared to the trench length.

Consistent with the concept that processes on one side of the slab do not significantly affect the dynamic pressure on the other side of the slab, the pressure outside the region of convergence and adjacent to the slabs remains low. As for the single slab systems, the dynamic pressures generated by the analytical method are in excellent agreement with numerical results.

Comparison between analytical and numerical results for other double subduction geometries, including double in-dip and double same-dip systems, is presented in section SG. Overall, the pressure is generally in very good to excellent agreement, including for geometries where one or both slabs subduct with an overturned geometry.

7. Discussion

This paper demonstrates a quantifiable link between the geometry and kinematics of plate and slabs and the associated distribution of dynamic pressure within the asthenosphere. We show that dynamic pressure and vertically averaged flow velocity for any depth-dependent (linear) viscosity can be encapsulated in two scalar parameters, a viscosity coefficient, C, and a coupling coefficient, β.

To build intuition, we derive analytical solutions for simple rectangular plate and slab geometries using the simplest possible form of the solutions. We show that, for systems without slabs, asthenospheric pressure differences, measured across a plate, generally scale with the shortest plate dimension. For systems with slabs, the pressure discontinuity across slabs (or slab walls) also scales generally with the shortest plate dimension. The exception is where parallel slabs are closely spaced and separated by distances that are small compared to trench length. Then, the pressure difference across slabs scales with the inverse of the separation distance between slabs and can become very large for closely spaced, rapidly converging slabs.

We also show that length scaling of the flow systems does not depend on the thickness of the asthenosphere or, in general, on the nature of the basal boundary conditions, except for the development of a narrowly defined boundary layer flow around subducting slabs, which has dimensions that scale with the channel thickness. These scaling relations provide a quantitative basis for interpreting the results of numerical modeling studies that explore the dependence of subduction dynamics and mantle flow regime on plate geometry (e.g., ; Schellart et al., 2007; Stegman et al., 2006, 2010) and more recently the dynamics of multiple, closely

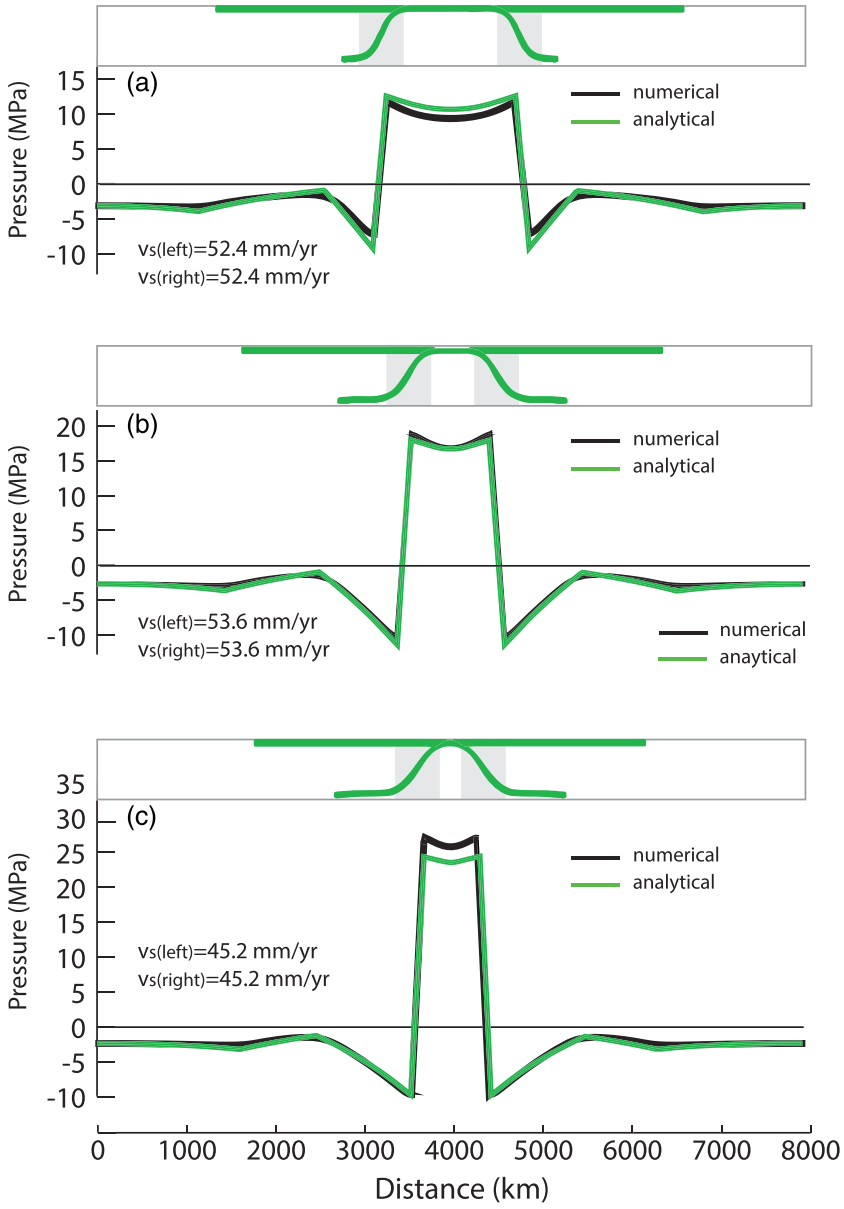

Figure 18. Numerically (black line) and analytically (green line) determined dynamic pressure for midline profiles through a double out-dipping subduction system undergoing progressive subduction. Trench length is 2,000 km, and slab geometry is as shown above each profile. Gray boxes show locations of the analytical slab regions. v_s is subduction velocity determined as the difference in plate velocity on either side of left and right trenches.

spaced subduction zones (e.g., Dasgupta & Mandal, 2018; Holt et al., 2017; Jagoutz et al., 2015; Király et al., 2018; Pusok & Stegman, 2019).

Another general principle demonstrated here, that tectonic processes that on one side of a slab wall have little effect on the asthenospheric velocity or dynamic pressure on the other side of the slab wall, also has obvious implications for mantle dynamics in regions with multiple slab boundaries. This is particularly applicable to the tectonic regime developed in the Western Pacific (e.g., Cížková & Bina, 2015; Faccenna et al., 2017; Holt et al., 2018), where complex slab geometries isolate individual regions of the mantle from one another.

We demonstrate that, if the relative velocities of plates and slabs are known, the dynamic pressure and vertically averaged velocity of the asthenosphere can be determined everywhere in a closed upper mantle

system. In addition, we show that dynamic pressure can be modified by some processes occurring at depth, such as by the presence of slab tails along the base of the upper mantle, as apparent at the Japan subduction zone (e.g., Li et al., 2008; Liu et al., 2017), and by the vertical flux of material from upper to lower mantle. Our simple examples illustrate how these additional components have predictable results for both asthenospheric pressure and the pressure difference across slabs.

We adapt this analytical approach to allow for multisegment boundaries, to produce dynamic pressures that are generally in very good to excellent agreement with numerical results for systems of single and double subduction. We show that Hele-Shaw flow provides the most accurate results when we apply a correction for boundary layer flow, whereby obstructions to flow in a viscous channel are padded outward by a distance equal to one third of the thickness of the channel. Using this scheme, we show that differences between analytical and 3-D numerical results are generally less than 1 MPa along pressure profiles that typically display variations in pressure of 10–20 MPa and up to 30–40 MPa for some double subduction systems.

Because uncertainties in the dynamic pressures computed by our method scale with the thickness of the channel, while the magnitude of the pressure field scales with trench length, the comparison of analytical and numerical results conducted in this paper is a stringent test of the analytical technique because of the small ratio of trench length to channel thickness. For the modeling of major Earth subduction systems, with much larger ratios of trench length to channel thickness, we expect the uncertainties arising from use of our analytical modeling technique to be very much smaller than the magnitude of the overall pressure field.

We have shown that dynamic pressure is quasi-symmetrical across convergent boundaries without slabs; it is the presence of slabs, which act as barriers to flow in the asthenosphere, that create discontinuity and asymmetry in dynamic pressure at convergent boundaries. This suggests that mantle circulation models that do not explicitly incorporate slabs will have difficulty in computing a dynamic pressure directly adjacent to subduction boundaries. Taken together with previous work relating slab dip and buoyancy to the pressure difference across subducting slabs (Holt et al., 2017; Figure 1), and Hager and O'Connell's (1978) original exploration of slab shapes within global flow computations, the results of this paper suggest that slab dip may be used as a barometer of dynamic pressure in the asthenosphere. This offers the possibility that slab dip can be used to constrain mantle flow models, as is the subject of a companion paper (Holt & Royden, 2020), which explores the interdependence of mantle flow and slab dip on a global scale.

Acknowledgments

We thank Boris Kaus, Clint Conrad, Valentina Magni, and an anonymous reviewer for detailed reviews that significantly improved the manuscript. The code used to solve for pressure and velocity using generalized plate boundary geometries (i.e., the multisegment approach of section 66) is available in the following online repository (https://doi.org/10.5281/zenodo.3785912).

References

Alisic, L., Gurnis, M., Stadler, G., Burstedde, C., & Ghattas, O. (2012). Multi-scale dynamics and rheology of mantle flow with plates. *Journal of Geophysical Research*, *117* (B10402). https://doi.org/10.1029/2012jb009234

Batchelor, G. (2000). *An introduction to fluid dynamics (Cambridge Mathematical Library)*. Cambridge: Cambridge University Press. https://doi.org/10.1017/CBO9780511800955

Buttles, J., & Olson, P. (1998). A laboratory model of subduction zone anisotropy. *Earth and Planetary Science Letters*, *164*(1-2), 245–262. https://doi.org/10.1016/s0012-821x(98)00211-8

Cížková, H., & Bina, C. (2015). Geodynamics of trench advance: Insights from a Philippine-Sea-style geometry. *Earth and Planetary Science Letters*, *430*, 408–415. https://doi.org/10.1016/j.epsl.2015.07.004

Cruciani, C., Carminati, E., & Doglioni, C. (2005). Slap dip vs. lithospheric age: No direct function. *Earth and Planetary Science Letters*, *238*(3–4), 298–310. https://doi.org/10.1016/j.epsl.2005.07.025

Dasgupta, R., & Mandal, N. (2018). Surface topography of the overriding plates in bi-vergent subduction systems: A mechanical model. *Tectonophysics*, *746*, 280–295. https://doi.org/10.1016/j.tecto.2017.08.008

Faccenna, C., Holt, A. F., Becker, T. W., Royden, L. H., & Lallemand, S. (2017). Dynamics of the Ryukyu/Izu-Bonin-Marianas double subduction system. *Tectonophysics*, *746*, 229–238. https://doi.org/10.1016/j.tecto.2017.08.011

Forsyth, D., & Uyeda, S. (1975). On the relative importance of the driving forces of plate motion. *Geophysical Journal of the Royal Astronomical Society*, *43*(1), 163–200. https://doi.org/10.1111/j.1365-246X.1975.tb00631.x

Fukao, Y., & Obayashi, M. (2013). Subducted slabs stagnated above, penetrating through, and trapped below the 660 km discontinuity. *Journal of Geophysical Research: Solid Earth*, *118*, 5920–5938. https://doi.org/10.1002/2013JB010466

Funiciello, F., Faccenna, C., & Giardini, D. (2004). Role of lateral mantle flow in the evolution of subduction systems: insights from laboratory experiments. *Geophysical Journal International*, *157*(3), 1393–1406. https://doi.org/10.1111/j.1365-246x.2004.02313.x

Gutenberg, B. (1959). *Physics of the Earth's interior*. New York: Springer.

Hager, B. H., & O'Connell, R. (1978). Subduction zone dip angles and flow driven by plate motion. *Tectonophysics*, *50*(2–3), 111–133. https://doi.org/10.1016/0040-1951(78)90130-0

Holt, A. F., & Royden, L. H. (2020). Subduction Dynamics and Mantle Pressure: (ii) Towards a Global Understanding of Slab Dip and Upper Mantle Circulation. *Geochemistry, Geophysics, Geosystems*, *21*, e2019GC008771 https://doi.org/10.1029/2019gc008771

Holt, A. F., Royden, L. H., & Becker, T. W. (2017). The dynamics of double slab subduction. *Geophysical Journal International*, *209*(1), 250–265. https://doi.org/10.1093/gji/ggw496

Holt, A. F., Royden, L. H., Becker, T. W., & Faccenna, C. (2018). Slab interactions in 3-D subduction settings: The Philippine Sea Plate region. *Earth and Planetary Science Letters*, *489*, 72–83. https://doi.org/10.1016/j.epsl.2018.02.024

Husson, L. (2012). Trench migration and upper plate strain over a convecting mantle. *Physics of the Earth and Planetary Interiors*, *212-213*, 32–43. https://doi.org/10.1016/j.pepi.2012.09.006

Jagoutz, O., Royden, L., Holt, A. F., & Becker, T. W. (2015). Anomalously fast convergence of India and Eurasia caused by double subduction. *Nature Geoscience*, *8*, 475–479. https://doi.org/10.1038/ngeo2418

Jarrard, R. D. (1986). Relations among subduction parameters. *Reviews of Geophysics*, *24*(2), 217–284. https://doi.org/10.1029/RG024i002p00217

Kincaid, C., Griffiths, & R. W. (2003). Laboratory models of the thermal evolution of the mantle during rollback subduction. *Nature*, *425*(6953), 58–62. https://doi.org/10.1038/nature01923

Király, Á., Capitanio, F. A., Funiciello, F., & Faccenna, C. (2016). Subduction zone interaction: Controls on arcuate belts. *Geology*, *44*(9), 715–718. https://doi.org/10.1130/G37912.1

Király, Á., Holt, A. F., Funiciello, F., Faccenna, C., & Capitanio, F. (2018). Modeling slab-slab interactions: Dynamics of outward dipping double-sided subduction systems. *Geochemistry, Geophysics, Geosystems*, *19*, 693–714. https://doi.org/10.1002/2017GC007199

Lallemand, S., Heuret, A., & Boutelier, D. (2005). On the relationships between slab dip, back-arc stress, upper plate absolute motion, and crustal nature in subduction zones. *Geochemistry, Geophysics, Geosystems*, *6*, Q09006. https://doi.org/10.1029/2005GC000917

Li, C., van der Hilst, R. D., Engdahl, R. E., & Burdick, S. (2008). A new global model for *P* wave speed variations in Earth's mantle. *Geochemistry, Geophysics, Geosystems*, *9*, Q05018. https://doi.org/10.1029/2007GC001806

Liu, X., Zhao, D., Li, S., & Wei, W. (2017). Age of the subducting Pacific slab beneath East Asia and its geodynamic implications. *Earth and Planetary Science Letters*, *464*, 166–174. https://doi.org/10.1016/j.epsl.2017.02.024

Moresi, L, & Gurnis, M (1996). Constraints on the lateral strength of slabs from three-dimensional dynamic flow models. *Earth and Planetary Science Letters*, *138*(1-4), 15–28. https://doi.org/10.1016/0012-821x(95)00221-w

Pusok, A. E., & Stegman, D. (2019). Formation and stability of same-dip double subduction systems. *Journal of Geophysical Research: Solid Earth*, *125*, 7387–7412. https://doi.org/10.1029/2018JB017027

Richards, M. A., Yang, W., Baumgardner, J. R., & Bunge, H. (2001). Role of a low-viscosity zone in stabilizing plate tectonics: Implications for comparative terrestrial planetology. *Geochemistry, Geophysics, Geosystems*, *2*(8). https://doi.org/10.1029/2000GC000115

Royden, L. H., & Husson, L. (2006). Trench motion, slab geometry and viscous stresses in subduction systems. *Geophysical Journal International*, *167*, 881–895.

Schellart, W. P. (2004). Kinematics of subduction and subduction-induced flow in the upper mantle. *Journal of Geophysical Research*, *109*(B07401). https://doi.org/10.1029/2004jb002970

Schellart, W. P., Freeman, J., Stegman, D. R., Moresi, L., & May, D. A. (2007). Evolution and diversity of subduction zones controlled by slab width. *Nature*, *446*, 308–311.

Stegman, D. R., Farrington, R., Capitanio, F., & Schellart, W. (2010). A regime diagram for subduction styles from 3-D numerical models of free subduction. *Tectonophysics*, *483*(1–2), 29–45.

Stegman, D. R., Freeman, J., Schellart, W. P., Moresi, L., & May, D. (2006). Influence of trench width on subduction hinge retreat rates in 3-D models of slab rollback. *Geochemistry, Geophysics, Geosystems*, *7*, Q03012. https://doi.org/10.1029/2005GC001056

Stevenson, D. J., & Turner, J. S. (1977). Angle of subduction. *Nature*, *270*, 334–336.

van der Hilst, R., Widiyantoro, S., & Engdahl, E. R. (1997). Evidence for deep mantle circulation from global tomography. *Nature*, *386*, 578–584.

Zhong, S. (2006). Constraints on thermochemical convection of the mantle from plume heat flux, plume excess temperature, and upper mantle temperature. *Journal of Geophysical Research*, *111*(B04409). https://doi.org/10.1029/2005jb003972